

REFRACTORY CARBIDES' MICROSTRUCTURAL INTEGRITY IN HOT HYDROGEN  
ENVIRONMENT OF SPACE NUCLEAR REACTORS

By

BRANDON WARREN CUNNINGHAM

A THESIS PRESENTED TO THE GRADUATE SCHOOL  
OF THE UNIVERSITY OF FLORIDA IN PARTIAL FULFILLMENT  
OF THE REQUIREMENTS FOR THE DEGREE OF  
MASTER OF SCIENCE

UNIVERSITY OF FLORIDA

2008

© 2008 Brandon Warren Cunningham

To the spark within humanity to defy conventional wisdom.

## ACKNOWLEDGMENTS

I first want to thank my mother, Tafferlon Ann Cunningham; and my grandparents, Minnie Lee and Willie Bud White, Sr. They have been and continue to be instrumental in making me the person I am today. I thank the supervisory committee members, Dr. Edward Dugan and Dr. Luisa Amelia Dempere. Special gratitude goes to my supervisory committee chair, Dr. Samim Anghaie, for giving me the opportunity to conduct this research. Dr Anghaie's knowledge of nuclear engineering is noteworthy of a true genius.

All experiments were conducted at the Applied Ultra High Temperature Research Laboratory of the Innovative Nuclear Space Power and Propulsion Institute (INSPI) at the University of Florida. Analysis was performed at the Major Analytical Instrumentation Center at the University of Florida.

## TABLE OF CONTENTS

	<u>page</u>
ACKNOWLEDGMENTS .....	4
LIST OF TABLES .....	7
LIST OF FIGURES .....	8
LIST OF ABBREVIATIONS.....	11
ABSTRACT.....	12
CHAPTER	
1 INTRODUCTION .....	14
2 BACKGROUND AND LITERATURE REVIEW .....	16
2.1 Historical Relevance for Fuel Development.....	16
2.1.1 Pewee Series .....	17
2.1.2 Nuclear Furnace Series .....	18
2.2 Literature Review.....	18
2.2.1 Hot Hydrogen Corrosion Mechanisms .....	18
2.2.2 Free Energy of Formation Calculations.....	19
3 EXPERIMENT METHODS AND PROCEDURES .....	24
3.1 Mass Flow Determination.....	24
3.2 Equipment and Testing Procedures .....	24
3.3 Specimen Preparation for Analysis.....	25
3.4 Analysis Methodology .....	27
4 RESULTS AND DISCUSSION .....	31
4.1 Mono-Carbides .....	31
4.1.1 Tantalum Carbide .....	31
4.1.2 Tungsten Carbide.....	32
4.1.3 Zirconium Carbide.....	34
4.2 Tri-Carbides .....	35
4.2.1 Bulk Carbon Analysis.....	35
4.2.2 XRD Analysis.....	36
4.2.3 SEM/EDS Analysis .....	36
5 CONCLUSIONS AND RECOMMENDATIONS .....	65

LIST OF REFERENCES .....67

BIOGRAPHICAL SKETCH .....69

LIST OF TABLES

<u>Table</u>	<u>page</u>
3-1 Average testing conditions for mono-carbide samples.....	28
3-2 Average testing conditions for tri-carbide samples .....	28
4-1 Uranium tri-carbide results .....	38
4-2 Uranium tri-carbide pre- and post-HHT carbon content.....	38

## LIST OF FIGURES

<u>Figure</u>	<u>page</u>
2-1 Four fuel forms used in Rover/NERVA designs (Matthews et al., 1991).....	21
2-2 Pseudo-binary phase diagram of $(U_{0.1}, Zr_{0.9})C_x$ (Lyon, 1973) .....	22
2-3 Standard free energy of formation of possible chemical reactions of mono-carbides in a hydrogen environment [8,9,10].....	23
3-1 Hot hydrogen test chamber .....	29
3-2 Top view of sample/tungsten susceptor/inductive coil configuration .....	29
3-3 Copper cooled induction coil with tungsten susceptor assembly .....	30
4-1 EDS of pre- and post-HHT TaC sample.....	39
4-2 Optical image of TaC. A) Pre-HHT TaC sample. B) Post-HHT TaC sample .....	39
4-3 TaC BSE image showing post-HHT cracking.....	40
4-4 TaC SE image showing fracture zone .....	40
4-5 TaC SE image of pre-HHT specimen.....	41
4-6 TaC SE image of post-HHT specimen .....	41
4-7 TaC bulk carbon content.....	42
4-8 Mid-axial cross section showing TaC carbon content as a function of depth .....	42
4-9 TaC pre- and post-HHT XRD spectrum.....	43
4-10 EDS of pre- and post-HHT of WC sample.....	43
4-11 Optical image of WC. A) Pre-HHT WC sample. B) Post-HHT WC sample.....	44
4-12 WC SE image of pre-HHT specimen .....	44
4-13 WC SE image of post-HHT specimen.....	45
4-14 WC bulk carbon content .....	45
4-15 WC BSE image showing the transition zone where carbon depletion occurred .....	46
4-16 Mid-axial cross section showing WC carbon content as a function of depth.....	46

4-17	Mid-axial cross section of post-HHT showing WC transition zone of carbon content.....	47
4-18	WC pre- and post-HHT XRD spectrum .....	47
4-19	EDS of pre- and post-HHT of ZrC sample.....	48
4-20	Optical image of ZrC. A) Pre-HHT ZrC sample. B) Post-HHT ZrC sample.....	48
4-21	ZrC SE image of pre-HHT specimen .....	49
4-22	ZrC SE image of post-HHT specimen.....	49
4-23	ZrC BSE image of pre-HHT specimen.....	50
4-24	ZrC BSE image of post-HHT specimen .....	50
4-25	ZrC bulk carbon content.....	51
4-26	Mid-axial cross section showing ZrC carbon content as a function of depth.....	51
4-27	ZrC pre- and post-HHT XRD spectrum .....	52
4-28	Optical image of TRI-C1. A) TRI-C1 pre-HHT. B) TRI-C1 post-HHT.....	53
4-29	Optical image of TRI-C2. A) TRI-C2 pre-HHT. B) TRI-C2 post-HHT.....	53
4-30	Optical image of TRI-C3. A) TRI-C3 pre-HHT. B) TRI-C3 post-HHT.....	54
4-31	Optical image of TRI-C4. A) TRI-C4 pre-HHT. B) TRI-C4 post-HHT.....	54
4-32	TRI-C1 pre- and post-HHT bulk carbon content.....	55
4-33	TRI-C2 pre- and post-HHT bulk carbon content.....	55
4-34	TRI-C3 pre- and post-HHT bulk carbon content.....	56
4-35	TRI-C4 pre- and post-HHT bulk carbon content.....	56
4-36	TRI-C1 XRD spectrum.....	57
4-37	TRI-C2 XRD spectrum.....	57
4-38	TRI-C3 XRD spectrum.....	58
4-39	TRI-C4 XRD spectrum.....	58
4-40	TRI-C1 BSE image of pre-HHT specimen.....	59
4-41	TRI-C1 BSE image of post-HHT specimen.....	59

4-42	TRI-C2 BSE image of pre-HHT specimen.....	60
4-43	TRI-C2 BSE image of post-HHT specimen.....	60
4-44	TRI-C3 BSE image of pre-HHT specimen.....	61
4-45	TRI-C3 SE image of post-HHT specimen.....	61
4-46	TRI-C4 BSE image of pre-HHT specimen.....	62
4-47	TRI-C4 BSE image of post-HHT specimen.....	62
4-48	TRI-C1 pre- and post-HHT EDS.....	63
4-49	TRI-C2 pre-and post-HHT EDS.....	63
4-50	TRI-C3 pre-and post-HHT EDS.....	64
4-51	TRI-C4 pre-and post-HHT EDS.....	64

## LIST OF ABBREVIATIONS

BSE	Backscattered Electron
C-wt%	Carbon Weight percent
EDS	Energy Dispersive Spectrum
EMPA	Electron Micro Probe Analysis
HHT	Hot Hydrogen Testing
HIP	Hot Isostatic Press
INSPI	Innovative Nuclear Space Power and Propulsion Institute
ISP	Specific Impulse
LANL	Los Alamos National Laboratory
MW <sub>th</sub>	Megawatt thermal
NASA MSFC	National Aeronautics and Space Administration Marshall Space Flight Center
NEP	Nuclear Electric Propulsion
NERVA	Nuclear Engine Rocket Vehicle Application
NF	Nuclear Furnace
NTP	Nuclear Thermal Propulsion
PyC	Pyrolytic-Carbon
SE	Secondary Electron
SEM	Scanning Electron Microscopy
TaC	Tantalum Carbide
WC	Tungsten Carbide
XRD	X-Ray Diffraction
ZrC	Zirconium Carbide
$\Delta G_f^\circ$	Standard free energy of formation

Abstract of Thesis Presented to the Graduate School  
of the University of Florida in Partial Fulfillment of the  
Requirements for the Degree of Master of Science

REFRACTORY CARBIDES' MICROSTRUCTURAL INTEGRITY IN HOT HYDROGEN  
ENVIRONMENT OF SPACE NUCLEAR REACTORS

By

Brandon Warren Cunningham

August 2008

Chair: Samim Anghaie

Major: Nuclear and Radiological Engineering

This project required the testing of three mono-carbides to investigate which carbide has the least degradation of microstructural properties when exposed to a hot hydrogen environment. This was performed in order to determine the usability of various carbides in a base mixture. The purpose of this research was to investigate carbides as candidate fuel matrix for nuclear thermal propulsion. Tantalum carbide (TaC), tungsten carbide (WC), and zirconium carbide (ZrC) were all tested in a hot hydrogen environment at an average temperature of 2775K. Each study tracked the carbon content, corrosion, density, hydrogen embrittlement, and phase changes. The results show that some carbides experienced changes in all of the aforementioned properties, while others experienced a combination of changes or no noticeable degradation.

The second stage of the research tested solid solution uranium bearing tri-carbides in a hot hydrogen environment. The tri-carbides included the compositions  $(U_{0.1}, Zr_{0.58}, Nb_{0.32})C_{0.95}$ ,  $(U_{0.1}, Zr_{0.68}, Nb_{0.22})C_{0.95}$ ,  $(U_{0.1}, Zr_{0.77}, Nb_{0.13})C_{0.95}$ , and  $(U_{0.05}, Zr_{0.62}, Nb_{0.33})C_{0.95}$ . All tri-carbides were exposed to temperatures above 2900K for two hours. Scanning electron microscopy, bulk carbon analysis, X-ray diffraction, density measurements, and mass measurements were used to characterize each specimen. Analysis showed that differences in metal composition had no

noticeable effect on final fuel integrity. Carbon analysis, electron microscopy, and diffraction analysis showed that tri-carbides displayed little to no change in microstructure due to exposure to a hot hydrogen environment.

## CHAPTER 1 INTRODUCTION

Fuel choice is a key element of nuclear reactors' use in space applications, particularly because of concerns about fuel performance. The nuclear thermal propulsion (NTP) and some nuclear electric propulsion (NEP) advanced space reactors must also consider the high temperature and high power density that the fuel experiences. Nuclear reactors intended for space applications will be required to achieve temperatures of 2500K or more. For NTP the high temperatures ensures high specific impulse (ISP) and for NEP efficient heat rejection. High melting point carbides or refractory carbides are capable of surviving these conditions for an extended prototypic core lifetime, making them a suitable fuel choice.

Refractory carbides have operating temperature estimated at 3000K. This high temperature capability makes them a preferred fuel choice, particularly when compared to other fuel candidates such as uranium dioxide, uranium carbide, or uranium nitride. The thermal conductivity of solid solution carbides approaches that of elemental uranium. This lowers the thermal gradient between the fuel and propellant, thus reducing thermal stress-induced cracking. The high thermal conductivity also allows for higher operating temperature with a smaller threat of fuel centerline melting. Carbides also exhibit low volatility, low density, and good neutronic properties such as good moderation due the presence of carbon and low absorption cross section.

A method for fabricating refractory carbides was established in previous research [1]. Solid solution uranium tri-carbides have been produced with the compositions (U,Zr,Nb)C, (U,Zr,Ta)C, (U,Zr,Hf)C, and (U,Ta,Nb)C. This paper will address how microstructural integrity changes by exposing tri-carbides to prototypic NTP/NEP temperatures. A hydrogen environment was examined because of its role in both types of systems: in NTP systems hydrogen is both the coolant and the propellant, while the NEP designs, such as the Pellet Bed

Reactor concept or Neptune reactor concept, it acts as a coolant. Uranium tri-carbide was chosen for testing because preliminary results showed that tri-carbides have higher melting temperatures and better resistance to hot hydrogen corrosion than the binary-carbide fuel (U,Zr)C [2].

Testing materials in a high temperature hydrogen environment is rare because most operating conditions do not warrant its use. As a result, background information and literature is limited. The main concern with NTP is hot hydrogen corrosion. Hydrogen at high temperatures can erode carbon from the matrix or react and corrode the fuel substrate to form methane or other hydrocarbons. Studies of previous NTP programs and case studies have shown that the hot hydrogen corrosion mechanisms are a highly coupled and highly complex process. Research shows that carbide's material properties are dependent on maintaining stoichiometry [3]. Changes in the fuel's carbon-to-metal ratio can lead to changes in the liquidus, changes in phase orientation, fatigue resistance, and toughness. A quantification of carbon-to-metal ratio with exposure time to temperature is needed to ensure properties such as melting point, thermal conductivity, and consistent thermal expansion are coherent throughout the fuel's anticipated lifetime. Evidence of hot hydrogen corrosion can show as hydrogen-induced blistering, hot embrittlement, mass loss, and hydride formation.

## CHAPTER 2 BACKGROUND AND LITERATURE REVIEW

### 2.1 Historical Relevance for Fuel Development

Nuclear reactors for rocket applications were first ground tested during the Rover program. The main purpose of the Rover program was to develop nuclear powered rockets for ballistic missile defense. When the need for nuclear rocket applications diminished due to the efficiency of chemical rockets, Los Alamos National Laboratory (LANL) contracted with Westinghouse Electric Corporation to create a research and development program within the original framework of the Rover program. The new program, the Nuclear Engine for Rocket Vehicle Applications (NERVA), was developed for space purposes. The NERVA program was charged not only with reactor design, but also to achieve the highest possible propellant temperature. The intent was a completed rocket design with maximized ISP while maintaining low weight.

Equation 1 defines ISP as proportional to the square root of the fluid temperature over the fluid molecular weight [2]. Hydrogen is the de facto coolant for NTP because its molecular weight is the lowest and highest specific heat of all elements. All parameters being equal, the temperature of the coolant dictates the efficiency of the rocket design. Therefore, fuel development was rigorously pursued in order to meet this goal. Throughout the course of the Rover program several reactors series with varying fuel forms were investigated. Figure 2-1 illustrates the fuels used during the Rover/NERVA program. Nuclear reactor cores developed during these programs generally operated with temperatures around 2500K and pressures of 3MPa. The series that is most important for this research, the Pewee and Nuclear Furnace families, focused on alternative fuels, higher fuel temperature, and fuel performance.

$$Isp = AC_f \sqrt{\frac{T_{ch}}{M_c}} = \frac{F}{\dot{m}} \quad \text{Eqn. 1}$$

A = performance factor related to thermo-physical properties of the propellant

C<sub>f</sub> = thrust coefficient, which is a function of nozzle parameters

T<sub>ch</sub> = chamber temperature (K)

M<sub>c</sub> = molecular weight of propellant

F = thrust (N)

m = mass flow rate of propellant (kg/s)

### 2.1.1 Pewee Series

The Pewee series was intended to be a family of small inexpensive test reactors used for high temperature fuels demonstration: only one reactor was eventually built and demonstrated. In 1968 the Pewee 1 ran successfully at 503MW<sub>th</sub> for 40 minutes with an exit coolant temperature of 2550K. The peak fuel temperature was measured at 2750K. It demonstrated the highest power for a reactor of its size, with an average power density of 2340 MW<sub>th</sub>/m<sup>3</sup> and a peak power density of 5200 MW<sub>th</sub>/m<sup>3</sup>. The calculated ISP in vacuum was 845s. Pewee contained 402 hexagonal fuel elements loaded with pyrolytic-graphite coated UC<sub>2</sub> particles dispersed throughout a graphite matrix. The fuel elements were coated with NbC, ZrC, and Mb as an overcoat. Inspection of the fuel elements after testing showed that many of the elements exhibited cracked regions or external corrosion. Fractures were due to thermal-mechanical stresses, but corrosion was attributed to the fuel elements' graphite matrix being subjected to a hot hydrogen environment [4].

### **2.1.2 Nuclear Furnace Series**

The Nuclear Furnace (NF) series had a purpose similar to the Pewee series. Like the Pewee 1, only one reactor in this series was built and operated. This was due to changes in national priorities, which forced the Rover/NERVA program to end in 1973. It was the last reactor built and tested during the Rover program. The NF 1 served as the test bed for two new types of fuel forms: (U,Zr)C composite and (U,Zr)C solid solution binary carbide. This was a 44MW<sub>th</sub> reactor that operated for 109 minutes with an average exit coolant temperature of 2450K. Unlike Pewee 1, this reactor contained 49 hexagonal fuel elements. For this test, the solid solution binary carbide fuel elements had no protective coating on the surface and showed minimal corrosion compared to the other fuel forms. It did, however, show extensive cracking. The composite performed better than the solid solution binary carbide in crack resistance but corrosion from hydrogen contacting the graphite matrix continued to be a problem [5].

## **2.2 Literature Review**

### **2.2.1 Hot Hydrogen Corrosion Mechanisms**

A review of past studies has shown that hot hydrogen corrosion is a highly complex and highly coupled process. That study showed that the corrosion process is a combination of the following: (1) exposure of the fuel to hot hydrogen gas, (2) thermal and mechanical cycling and loading, (3) radiation induced damage to the fuel matrix, and (4) annealing effect from high temperature creep [6]. The first process is responsible for the corrosion of the microstructure. The last three mechanisms influenced the rate at which the fuel matrix was degraded.

Hydrogen is able to penetrate the microstructure through micro-cracks and surface pores. Depending on the local conditions such as local temperature, pressure, and composition a free energy change or chemical reaction can occur and give rise to hydrocarbon reaction products. Typically, reaction products occupy a greater volume than the reactants. This causes stress-

corrosion cracking, which consequently creates a larger surface area and deeper route for the hot hydrogen to attack. The corrosion-induced cracks and pores weaken the microstructure and allow for surface erosion. The depletion of carbon from the fuel surface leads to changes in local composition, which alters local material properties. In solid solution uranium bi-carbides it has been shown that material properties depend heavily on the carbon-to-metal ratio. Figure 2-2 shows a phase diagram of a pseudo-binary carbide  $(U_{0.1}, Zr_{0.9})C_x$ . In this composition the carbon-to-metal ratio is limited to 0.92-0.96 before a solid fuel transforms to a mixture of liquid/solid solution carbide. Allowing this to occur will ultimately lead to fuel failure.

Fuel irradiation enhances the rate of hot hydrogen corrosion. Exposure of the microstructure to radiation, particularly fast neutrons, creates lattice dislocations and point defects. The localized defect effectively reduces the local thermal conductivity which produces a thermal gradient with the surrounding lattice sites. The defects also reduce local ductility. This, combined with the reduction in thermal conductivity, produces thermal stress-induced cracking that exposes more surface area to hot hydrogen attack.

Creep is a mechanism that does not enhance the hot hydrogen corrosion rate, unlike the other two processes. The operating temperatures of NTP fuel accelerate the creep process. Creep will serve to anneal the localized high stress zones deterring the formation of crack growth and closing micro-cracks within the microstructure.

### **2.2.2 Free Energy of Formation Calculations**

Binary carbides and ternary carbides are materials whose full use has yet to be investigated. As a result, there is no tabulated data on the free energy of formation to determine the system's thermodynamic stability. The free energy of formation for the mono-carbides was calculated to determine the system's stability in a hydrogen environment. An approximation of

ternary carbide system stability was made by observing the Gibbs potential for mono-carbides since uranium tri-carbide is a solid solution of (U,Zr,X)C where X is a metal.

The second law of thermodynamics was used to determine whether the mechanism for microstructural damage to mono-carbides was predominantly corrosion or erosion. The Standard Free Energy of Formation ( $\Delta G_f^\circ$ ) gives the work released or consumed by a chemical reaction at constant temperature and pressure. If  $\Delta G_f^\circ$  is positive the chemical reaction is non-spontaneous and if  $\Delta G_f^\circ$  is negative the chemical reaction is spontaneous. A positive  $\Delta G_f^\circ$  means that the species reaction cannot take place under the given conditions without the minimum of the  $\Delta G_f^\circ$  calculated [7]. The  $\Delta G_f^\circ$  was calculated for several chemical reactions that are possible in a hydrogen environment, neglecting the presence of trace elements such as oxygen in the testing system. The dissociation energy of diatomic hydrogen is 4.5eV. This is higher than the thermal energy of the system, 2700K or 0.232eV. For simplification, only atomic hydrogen would be considered because of its chemical volatility. Figure 2-3 displays the Gibbs free energy plot for several reactions. With the exception of one chemical reaction each of the other reactions are not possible at the temperatures of interest without the addition of more work. This implies that the main mechanism for microstructural damage is erosion rather than corrosion. The one chemical reaction that is spontaneous is  $WC+4H \rightarrow W+CH_4$ , which readily occurs at temperatures beneath 445K or its equilibrium temperature. This is a reaction that is plausible for corrosion to occur and carbon loss to be significant. Using this principle the mono-carbide, WC, should experience a noticeable loss in carbon content. Since erosion is the mechanism for damaging the TaC and ZrC matrix those compounds could exhibit a uniform loss of both metal and carbon.

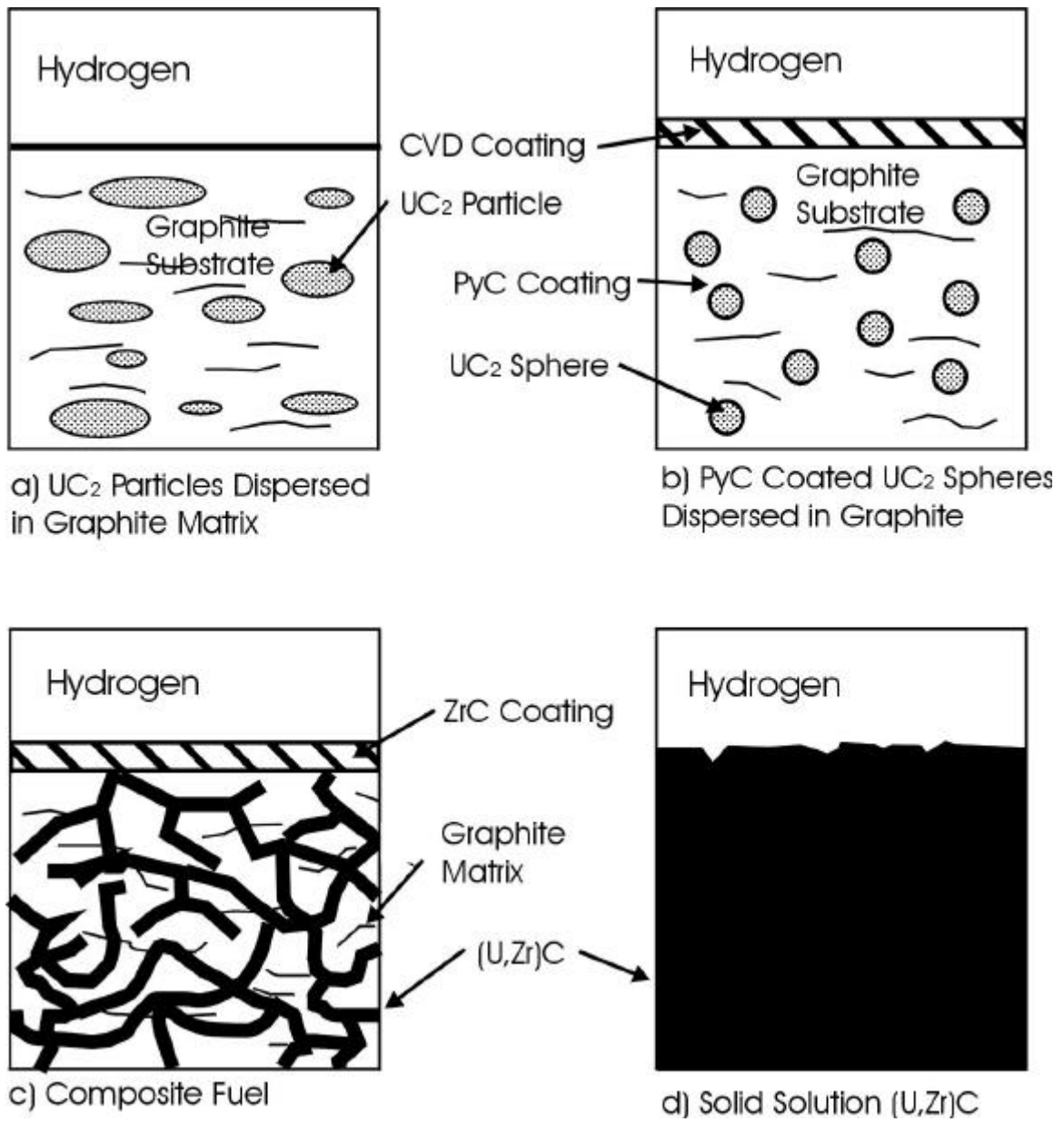


Figure 2-1. Four fuel forms used in Rover/NERVA designs (Matthews et al., 1991)

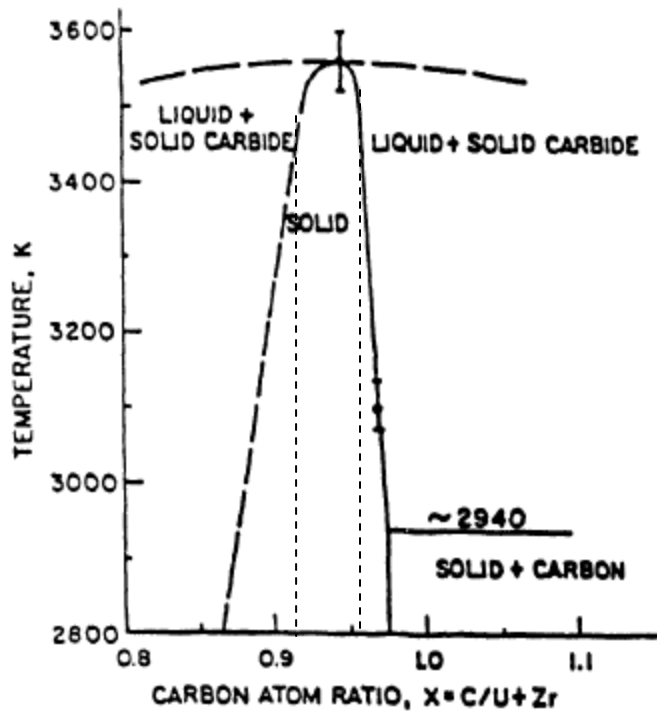


Figure 2-2. Pseudo-binary phase diagram of  $(U_{0.1}, Zr_{0.9})C_x$  (Lyon, 1973)

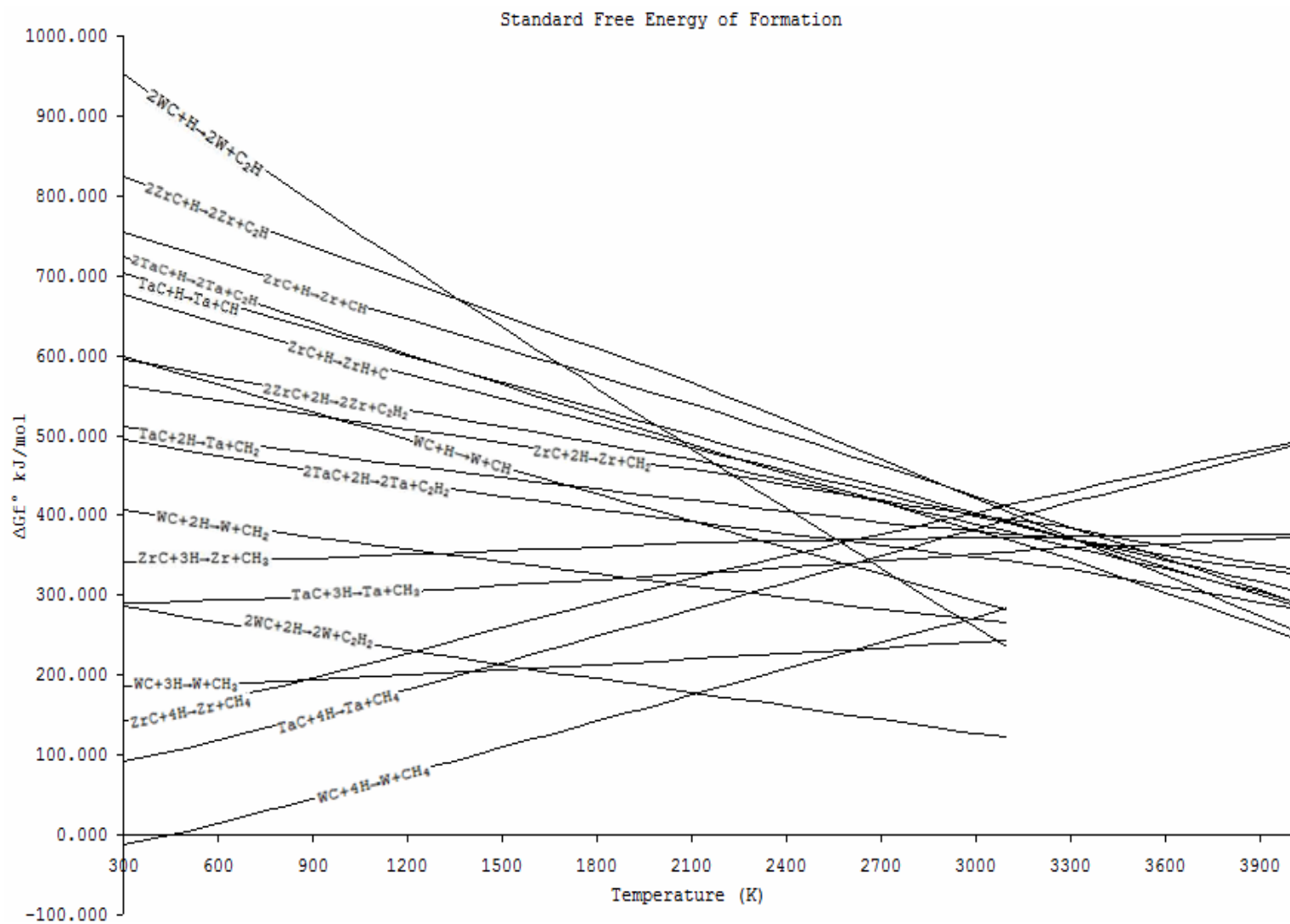


Figure 2-3. Standard free energy of formation of possible chemical reactions of mono-carbides in a hydrogen environment [8,9,10]

## CHAPTER 3 EXPERIMENT METHODS AND PROCEDURES

### 3.1 Mass Flow Determination

A linear relationship was used to ensure that the samples tested in this experiment experienced a relative mass flow rate similar to a nuclear space reactor. The Pewee reactor from the Rover/NERVA program was used as a template. The Pewee reactor used a total hydrogen flow rate of  $19.341 \frac{kg}{s}$  with  $14.62 \frac{kg}{s}$  cooling the fuel. The total available coolant area of  $858,929 \text{cm}^2$  was based on dimensions of the core [4]. This gives a mass flow per square centimeter of  $7.9401 \times 10^{-5} \frac{kg}{s \cdot \text{cm}^2}$ . The mono-carbide and tri-carbide specimen tested in this experiment had an available coolant area of approximately  $3.5 \text{cm}^2$  resulting in an equivalent mass flow rate of  $2.71 \times 10^{-4} \frac{kg}{s}$ . The dimensions of each specimen vary slightly making  $3.5 \text{cm}^2$  the estimated sample surface the coolant contacts. Chamber pressure, temperature, and mass flow rate were recorded every 10 minutes to calculate and average testing conditions. All average testing conditions are listed in tables 3-1 and 3-2.

### 3.2 Equipment and Testing Procedures

Two series of samples were tested. Mono-carbide samples produced at National Aeronautics and Space Administration's Marshall Space Flight Center (NASA MSFC) and uranium tri-carbides produced at University of Florida's Innovative Nuclear Space Power and Propulsion Institute (INSPI). The mono-carbides were fabricated by hot Isostatic press (HIP). Tri-carbides were fabricated by an induction heated uni-axial hot press liquid phase sintering method [1]. During this process a homogeneous mixture of three carbides are cold pressed and heated to a temperature above the lowest melting point carbide constituent, in this case uranium carbide. The liquid uranium carbide fills in porous areas and contacts the grain boundary from

other the carbide component, thereby quickening the diffusion and resulting in a solid solution tri-carbide fuel.

Figure 3-1 illustrates the hot hydrogen test equipment utilized to create the desired conditions. Samples were placed in a chamber that is evacuated to a maximum 100millitorr then backfilled with hydrogen in order to purge the system of oxygen and other gas impurities. This was performed three times to minimize oxidation of the sample and chamber components. The system was then purged and filled with hydrogen to the positive pressure, with respect to atmospheric pressure, to ensure air could not enter the chamber. The pressure was monitored with an Omega pressure transducer. The experiment was powered by a LEPEL Solid State RF generator. Ultra pure hydrogen then flowed from a gas cylinder through the system for a prototypic NTP run time. Hydrogen flow rate was measured by an OMEGA FMA-873 mass flow controller. The temperature was monitored through the use of a MAXLINE IRCON active control and measured by a MAXLINE IRCON two color infrared pyrometer. The pyrometer was aligned with a viewport on the chamber to allow observations to be made. The sample was surrounded by a tungsten susceptor that was inductively heated by a water-cooled copper coil surrounding the tungsten susceptor. The sample was heated via radiative heat transfer from the tungsten susceptor. Figure 3-2 shows the sample-coil assembly housed in the vacuum chamber. Figure 3-3 shows the coil assembly with the hole drilled through the tungsten susceptor to allow the pyrometer to measure the inner surface wall of the tungsten susceptor. This provided a more accurate representation of the specimen temperature. A parametric temperature study, up to 2573K, was made with a C-type thermocouple to ensure accuracy of pyrometer readings.

### **3.3 Specimen Preparation for Analysis**

After testing was complete the samples were prepared for microstructural characterization. First, the test samples were sectioned with a LECO® VC-50 diamond saw. A diamond blade was used

to account for the hardness of carbides. Individual sections were taken for X-ray Diffraction (XRD), bulk carbon analysis, Electron MicroProbe Analysis (EMPA), and Scanning Electron Microscope (SEM) analysis. All specimens were ultrasonically cleaned and degassed in distilled water for 60 minutes with a Branson® B3-R. All specimens were dried in a desiccator for a minimum of 24 hours before the analysis was conducted.

*a. XRD Preparation*

- i. Specimens were either pulverized to a powder in an alumina crucible or sectioned to approximately 0.5mm thickness and mounted on glass slides using a Amyl acetate and Collodian solution.

*b. Bulk Carbon Analysis*

- i. Specimens prepared for bulk carbon analysis were pulverized to a powder in an alumina crucible.
- ii. Three to five batches weighing 0.25g from each sample composition were placed in a zirconia crucible. High purity accelerator was added to ensure samples could be inductively heated and ignited. A mixture of 1.8g of copper and 1.2g of iron were the amounts recommended by the equipment's operations manual. The iron carbon impurity content was 8PPM.
- iii. Samples were placed in carbon analyzer for combustion analysis. The carbon determinator was calibrated using a tungsten carbide standard with 6.18wt% C.

*c. SEM and EMPA Preparation*

- i. Sections for SEM and EMPA were mounted in phenol ring molds using a 1:5 ratio LECO hardener to LECO epoxy resin, respectively.
- ii. LECO® Spectrum System 1000 with semi-automatic heads was used for rough polishing mounted specimens from 180grit to 1200grit.
- iii. The final polishing steps decreased surface roughness from 15µm to 0.5µm. Polishing was performed by hand.
- iv. Sections intended for SEM were acid etched for one minute with HNO<sub>3</sub>/HCl/H<sub>2</sub>SO<sub>4</sub> solution.
- v. Sections intended for EMPA was not acid etched.

### 3.4 Analysis Methodology

The following variables were examined for pre- and post-hot hydrogen testing (HHT): overall carbon concentration, carbon and metal concentration as a function of depth, density, and phase and crystallographic changes. Several visual observations such as grain growth, inter and intra-granular corrosion or erosion, spallation, cracking, swelling, and hydrogen embrittlement were also made. The pre- and post-HHT density was measured by immersion testing. A LECO WC-200 carbon determinator was used to combust specimens to investigate the bulk carbon concentration. A carbon profile of each specimen as a function of depth was characterized by EMPA. The EMPA instrument used was a JEOL SUPERPROBE 733 Electron Probe. Topographical and compositional contrast and elemental composition were inspected with a JEOL JSM-6400 SEM. SEM was conducted to make most visual observations. Using XRD, phase and crystallographic properties were analyzed with Philips APD 3720 X-Ray Diffractometer and reference spectra database [11]. Specimen weight and dimensions were measured with the Sartorius R180D analytic balance with an accuracy of 0.00001g and a Mitutoyo Absolute Digimatic Caliper (CD-6" CSX), respectively.

Table 3-1. Average testing conditions for mono-carbide samples

	TaC	WC	ZrC	
<i>Mass Flow Rate</i>	15.58	15.19	15.74	<i>g/min</i>
<i>Temperature</i>	2762	2779	2776	Kelvin
<i>Chamber Pressure</i>	968	969	970	torr
<i>Run Time</i>	2	2	1.167*	hr

\*The ZrC sample test was conducted for a shorter time because of equipment constraints.

Table 3-2. Average testing conditions for tri-carbide samples

	$(U_{0.1}, Zr_{0.58}, Nb_{0.32})C_{0.95}$	$(U_{0.1}, Zr_{0.68}, Nb_{0.22})C_{0.95}$	$(U_{0.1}, Zr_{0.77}, Nb_{0.13})C_{0.95}$	$(U_{0.05}, Zr_{0.62}, Nb_{0.33})C_{0.95}$	
<i>Mass Flow Rate</i>	15.81	14.92	14.92	14.92	<i>g/min</i>
<i>Temperature</i>	2926	2903	2903	2903	kelvin
<i>Chamber Pressure</i>	982	964	964	964	torr
<i>Run Time</i>	2	2	2	2	hr



Figure 3-1. Hot hydrogen test chamber

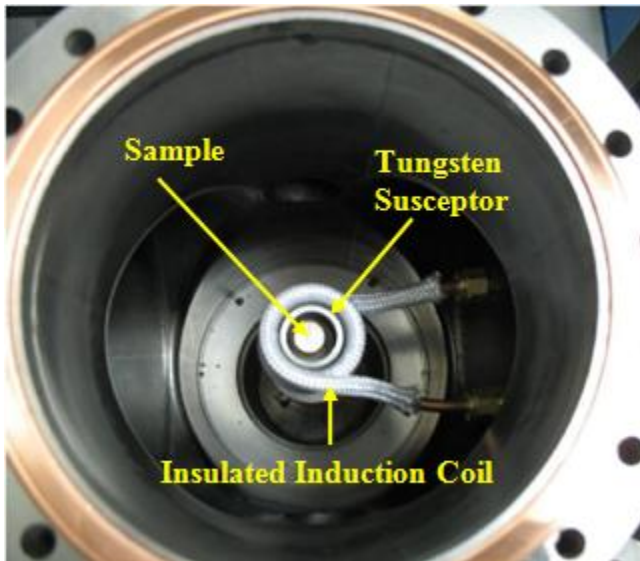


Figure 3-2. Top view of sample/tungsten susceptor/inductive coil configuration

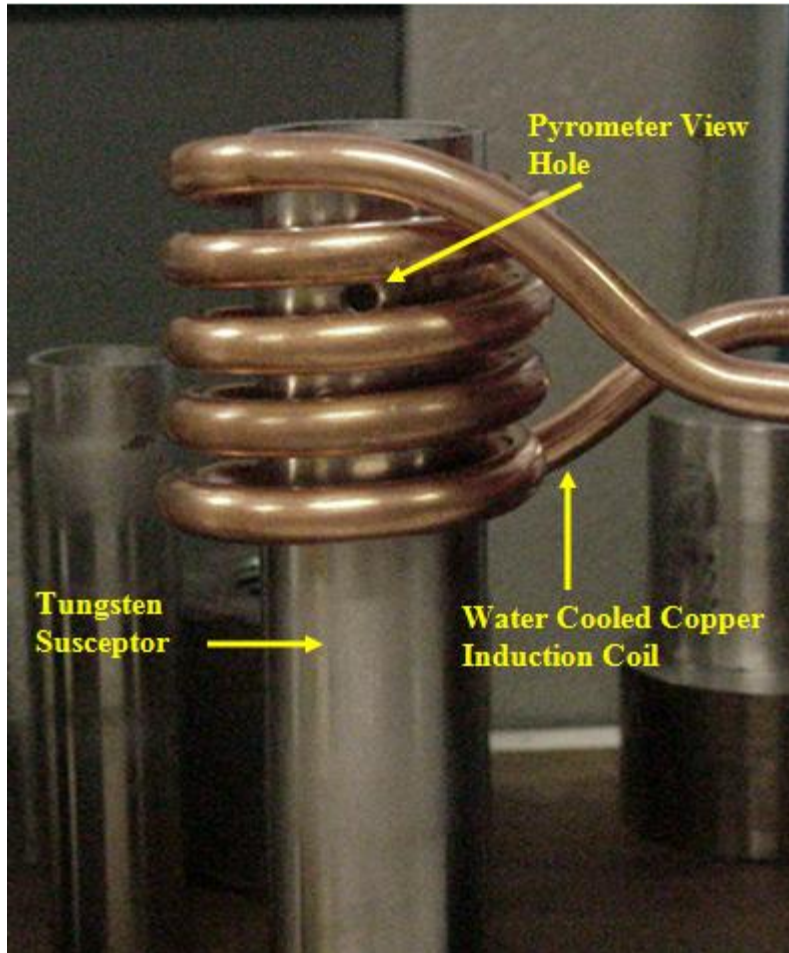


Figure 3-3. Copper cooled induction coil with tungsten susceptor assembly

## CHAPTER 4 RESULTS AND DISCUSSION

### 4.1 Mono-Carbides

#### 4.1.1 Tantalum Carbide

To begin the analysis an energy dispersive spectrum (EDS) was taken to verify that the sample contains the given elements. Figure 4-1 shows the EDS both pre- and post-HHT. The post-HHT spectrum was taken to verify there was no contamination—atomic numbers higher than carbon—were introduced to the sample after HHT. Figure 4-2 gives a view of the pre- and post-HHT TaC samples. Compared to the pre-HHT sample, the post-HHT shows extensive cracking on the surface. A cross section was taken through the post sample and subsurface cracking was also present. Figures 4-3 and 4-4 show the extent of cracking through a mid-axial cross-section. Figures 4-5 and 4-6 show that the grain structure was unaffected by the presence of hydrogen. Neither grain growth nor grain degradation occurred, but the grain area adjacent to the cracks was fractured. Fractures could be attributed to fast heat up rate.

TaC has a theoretical carbon weight percent (C-wt%) of 6.224wt%.. Figure 4-7 shows the pre-HHT C-wt% at 8.136wt% and post-HHT at 7.975wt%, both of which are hyper-stoichiometric. Statistically there was no change in carbon content. To determine if that small difference in the mean C-wt% for the pre- and post-HHT samples is due to the depletion of carbon at the surface from hydrogen flow, an EMPA was performed. The results of the EMPA shown in figure 4-8 illustrates that the pre- and post-HHT samples show no change in carbon concentration from the surface of the sample to within 360 $\mu$ m. The data point at 400 $\mu$ m represents the center of the sample or 3mm from the edge. The fluctuation in the EMPA profile is caused by surface roughness. The surface roughness scatters the incident electrons in directions that exaggerate or decrease the counts in the solid angle of the detector.

The immersion density test showed that for the TaC pre-HHT sample the density was  $14.350 \text{ g/cm}^3$ . The post-HHT sample had  $13.656 \text{ g/cm}^3$  yielding a percent change of 4.836%. The reference theoretical density for TaC is  $14.498 \text{ g/cm}^3$  making the pre-HHT sample 98.98% dense and the post-HHT sample 94.19% dense after a two hour run time. Since pores are often the sites for crack initiation it is possible that pores are the cause of the extensive cracking throughout the TaC sample.

The XRD analysis for the pre- and post-HHT showed that the structure did not undergo a phase change. Figure 4-9 displays the results. If any of the reactions in figure 2-3 would have occurred, peaks indicating elemental tantalum would have been present.

#### **4.1.2 Tungsten Carbide**

The EDS displayed in figure 4-10 indicates that the elemental compositions for the pre- and post-HHT samples are consistent. The other analysis for the post-HHT sample shows a large difference in properties from the pre-HHT. The blistering on the surface in figure 4-11b indicates the formation of a liquid or a gas. Assuming there were trace amounts of oxygen in the system and the formation of tungsten oxide was negligible, the blistering on the surface could be attributed to trapped methane gas. The post-HHT WC sample shows that the degradation occurred at the grain boundaries. An explanation for the blistering can be attributed to the Gibbs potential calculated for WC. Hydrogen reacted with carbon in the WC matrix forming methane or hydrocarbons. That methane gas then diffuses through the path of least resistance or the boundaries to the surface. The gas that did not escape was trapped under the surface to blister. Significant grain growth occurred in the WC sample. Figure 4-12 and figure 4-13 show the pre-HHT and post-HHT grain structure respectively. This can be attributed to conducting the testing near the melting point of tungsten carbide (3143K).

Figure 4-14 indicates that the bulk carbon content for the pre-HHT sample was 12.7% while the post-HHT sample had a C-wt% of 5.928. Since pre-and post-HHT carbon content are outside of their statistical error then depletion of carbon from the microstructure occurred with certainty. The large difference in the pre- and post-HHT carbon content was due to carbon depletion at the surface of the WC in the post-HHT sample. Figure 4-15 shows a BSE image of the WC post-HHT. The brighter edge region indicates there was higher tungsten content at the edge. The depletion of carbon at the edge was verified using EMPA. Figure 4-16 shows that the post-HHT sample has less carbon content within the first 360 $\mu$ m from the edge. The data point at 400 $\mu$ m represents the center or 3mm from the edge of the sample. That data point at the center of the sample indicates there is a diffusion gradient of carbon in the post-HHT sample. Figure 4-17 illustrates that at a depth of 630 $\mu$ m, the WC post-HHT sample's depleted carbon zone returns to the carbon concentration of the pre-HHT sample. This gives a carbon depletion depth rate approximately  $5.25 \frac{\mu\text{m}}{\text{min}}$ .

Notice the difference between the pre-HHT bulk 12.7C-wt% and EMPA's pre-HHT average trend which shows a lower C-wt%. Figure 4-15 shows dark spherical regions rich in carbon that would have been included in the bulk carbon analysis but not the EMPA result. Therefore the C-wt% for the WC matrix follows the EMPA trend, average 7.75wt%, but the sample's C-wt% is 12.7%. These rich carbon regions were probably introduced during the sample's fabrication as contamination. There is a large difference in the pre- and post-HHT density. The pre-HHT density is  $15.873 \frac{\text{g}}{\text{cm}^3}$  while the post-HHT sample is  $14.141 \frac{\text{g}}{\text{cm}^3}$ . This gives a percent difference of 10.91%.

The XRD spectrum shows that there were significant changes in phase. The pre-HHT sample in figure 14-18 illustrates that only the WC phase is present. The post-HHT sample reveals the presence of two phases: WC and W<sub>2</sub>C. The presence of the W<sub>2</sub>C is evidence that the carbon-to-metal ratio has decreased due to depletion of carbon from the microstructure surface.

#### 4.1.3 Zirconium Carbide

The EDS for the ZrC pre- and post-HHT samples are displayed figure 4-19. The results show that both samples' composition is consistent throughout the experiment. Figure 4-20a and 4-20b shows that on the surface the post-HHT sample displays little to no changes when compared to the pre-HHT sample. There is a slight discoloration caused by hot hydrogen etching the carbonaceous or loose material on the surface. Figures 4-21 and 4-22 show that qualitatively the microstructure was unchanged. The BSE images in 4-23 and 4-24 show no compositional differences or any depleted carbon regions due to hydrogen flow.

A bulk carbon analysis confirmed the qualitative result of an unchanged post-HHT ZrC microstructure. Figure 4-25 illustrates the pre-HHT C-wt% valued at 16.450wt% and the post-HHT C-wt% valued at 16.775wt%. Though the post-HHT sample is higher, the values are within close statistical error. The theoretical ZrC carbon content is 11.634wt%. The EMPA in figure 4-26 shows that there was no depletion of carbon at the surface of the sample. The variability in data points is caused by surface roughness.

Changes in density could reveal the presence of hydrogen embrittlement. The pre-HHT sample's density was  $6.648 \frac{g}{cm^3}$ , while the post-HHT sample's density was  $6.635 \frac{g}{cm^3}$ . The change in density from the control sample is 0.197%. Given the precision of the immersion testing, the values of the pre- and post-HHT density are statistically the same.

The XRD analysis was the last test to confirm an unchanged microstructure. The pre and post-HHT ZrC samples illustrated in figure 4-27 show that the peak-to-peak positions are unmoved, indicating the structure underwent little to no change.

## **4.2 Tri-Carbides**

Four uranium tri-carbide compositions were tested in a hot hydrogen environment. The carbon-to-metal ratio was fixed at 0.95. The primary goal was to examine depletion of carbon from the microstructure, but the investigation also considered how differing the metal atom fraction could affect the microstructure's integrity. The four tri-carbide compositions were pre-determined by previous research [1].

Tri-carbide sample designations, compositions, and changes in density and mass are listed in table 4-1. All of the tri-carbides displayed a mass loss as a result of the two hour hot hydrogen test. This was expected to occur because of vaporization of material species from the surface. Figures 4-28 through 4-31 are optical microscope images of each tri-carbide before and after testing. No signs of surface degradation such as partial melting of individual carbide constituent or hydrogen-induced blistering or cracking were observed.

### **4.2.1 Bulk Carbon Analysis**

Bulk carbon analysis for each tri-carbide is given in figures 4-32 through 4-35 and table 4-2. With the exception for of TRI-C4, the other specimens' post-HHT carbon content were within error of the pre-HHT carbon content and no change occurred from the flow of hydrogen. The decrease of TRI-C4's carbon content can be explained by observing TRI-C4's pre-HHT SEM image in figure 4-46. TRI-C4 showed excessive porosity, implying the specimen had not undergone significant densification before HHT. The post-HHT samples illustrate the specimen underwent a large degree of sintering due to exposure to the 2900K temperature. Figure 4-35 showed TRI-C4's initial carbon content at 11.775%. The high carbon content was most likely

due to carbonaceous material contaminating the surface and filling the pores. Samples TRI-C1, TRI-C2, and TRI-C3 showed no measurable decrease in carbon content implying little to no erosion or corrosion of carbon from the tri-carbide matrix occurred. The bulk carbon analysis demonstrated that the tri-carbides' carbon content remain close to stoichiometric weight percent

#### **4.2.2 XRD Analysis**

Another measure of changes in the microstructure would have been revealed through XRD. None of the post-HHT diffraction patterns in figures 4-36 through 4-39 showed the presence of different phases from that of the pre-HHT samples' diffraction pattern. The structure was considered to be a solid solution because the diffraction pattern did not exhibit the presence of segregated carbide constituents. Observing the XRD pattern of NbC, ZrC, and UC/UC<sub>2</sub> powders from a previous research [1], the diffraction pattern of the tri-carbides verified that a solid solution of (U,Zr,Nb)C exists in both the pre- and post-HHT specimens. No changes in phase or crystallographic orientation occurred as a result of the two hour test at 2900K.

#### **4.2.3 SEM/EDS Analysis**

Using SEM, compositional contrast and topographical images were obtained. Figures 4-40 through 4-47 are images of the specimens' microstructure. Heterogeneity of Zr and Nb in the microstructure could not be ascertained from BSE images due to the proximity of their atomic numbers. It can be inferred that had the pre- and post-HHT XRD patterns displayed ZrC and NbC spectra, the two elements would have been segregated in the microstructure. Knowing that this was not the case, Zr and Nb could be assumed to have a homogeneous distribution. Based on compositional contrast images, all the tri-carbides displayed no regions of depleted carbon or a gradient of uranium from the surface. In addition to SEM images, EDS was taken of each pre- and post-HHT sample to ensure no contamination was introduced to the sample during testing or

analysis preparation. Qualitative elemental composition for each tri-carbide is shown in figures 4-48 through 4-51.

Table 4-1. Uranium tri-carbide results

Sample Designation	Tri-carbide composition (atom fraction)	Pre-HHT Density (g/cm <sup>3</sup> )	Post-HHT Density (g/cm <sup>3</sup> )	Relative density difference	Pre-HHT Mass (g)	Post-HHT Mass (g)	Mass Difference (g)	Percentage of mass loss
<i>TRI-C1</i>	(U <sub>0.1</sub> , Zr <sub>0.58</sub> , Nb <sub>0.32</sub> )C <sub>0.95</sub>	6.1066	5.7567	-5.73%	2.24545	2.11287	-0.13258*	-5.9%
<i>TRI-C2</i>	(U <sub>0.1</sub> , Zr <sub>0.68</sub> , Nb <sub>0.22</sub> )C <sub>0.95</sub>	6.5306	6.1129	-6.40%	2.53249	2.43116	-0.10133*	-4.0%
<i>TRI-C3</i>	(U <sub>0.1</sub> , Zr <sub>0.77</sub> , Nb <sub>0.13</sub> )C <sub>0.95</sub>	6.2807	6.4215	+2.24%	2.85000	2.81581	-0.03416*	-1.2%
<i>TRI-C4</i>	(U <sub>0.05</sub> , Zr <sub>0.62</sub> , Nb <sub>0.33</sub> )C <sub>0.95</sub>	6.2961	6.9031	+9.64%	4.83599	4.70004	-0.12561*	-2.81%

\* A negative value implies a loss occurred. A positive value implies a gain occurred

Table 4-2. Uranium tri-carbide pre- and post-HHT carbon content

Sample Designation	Theoretical Carbon Content (wt %)	Pre-HHT Carbon Content (wt%)	Post-HHT Carbon Content (wt%)
TRI-C1	9.689	10.875	11
TRI-C2	9.700	0.9375	9.9425
TRI-C3	9.710	9.93	9.725
TRI-C4	10.32	11.775	10.35

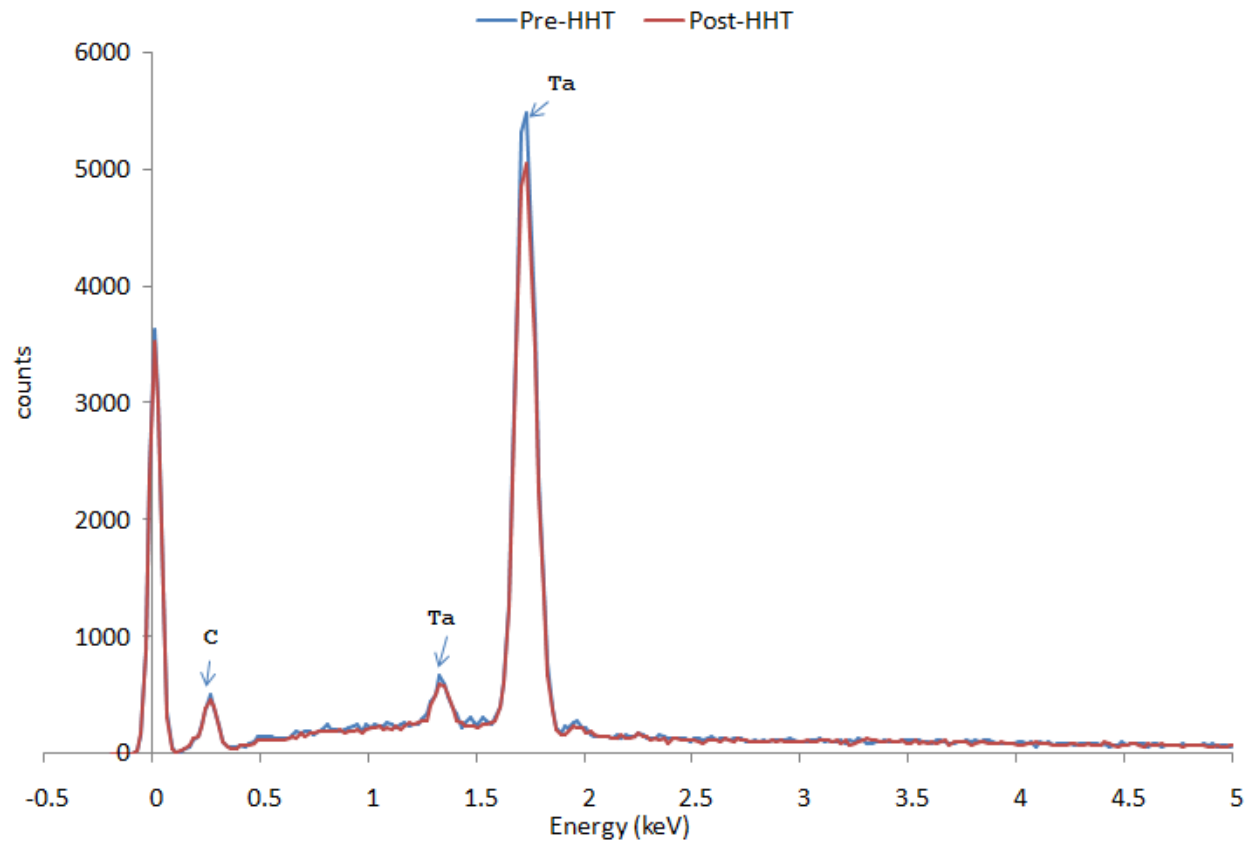


Figure 4-1. EDS of pre- and post-HHT TaC sample

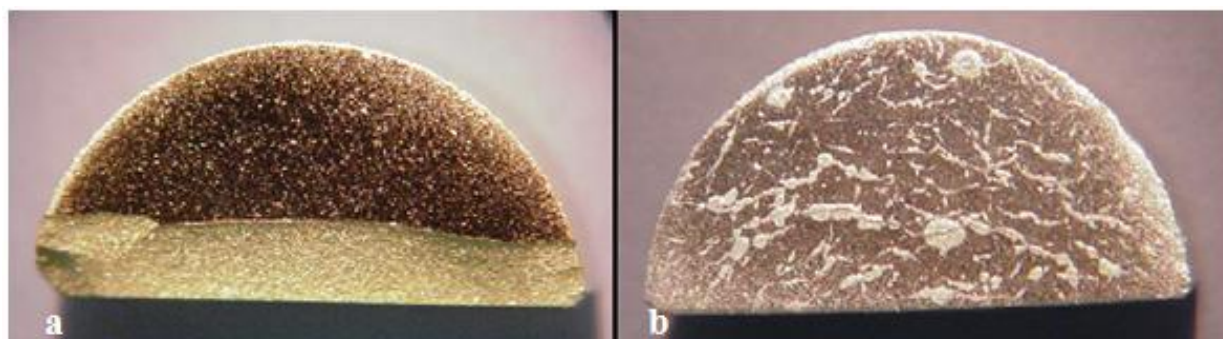


Figure 4-2. Optical image of TaC. A) Pre-HHT TaC sample. B) Post-HHT TaC sample

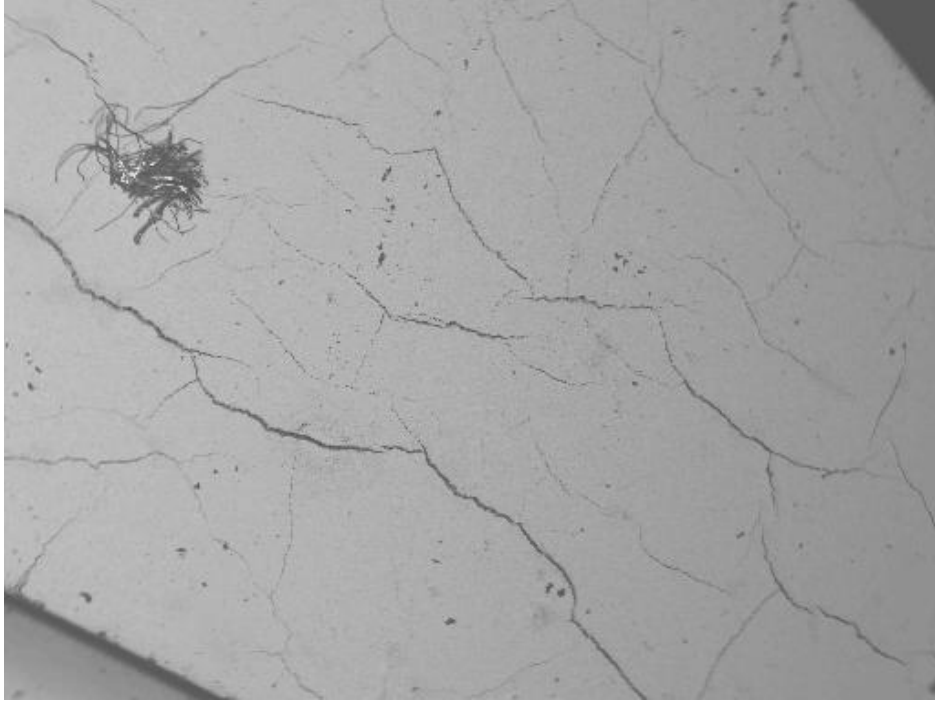


Figure 4-3. TaC BSE image showing post-HHT cracking

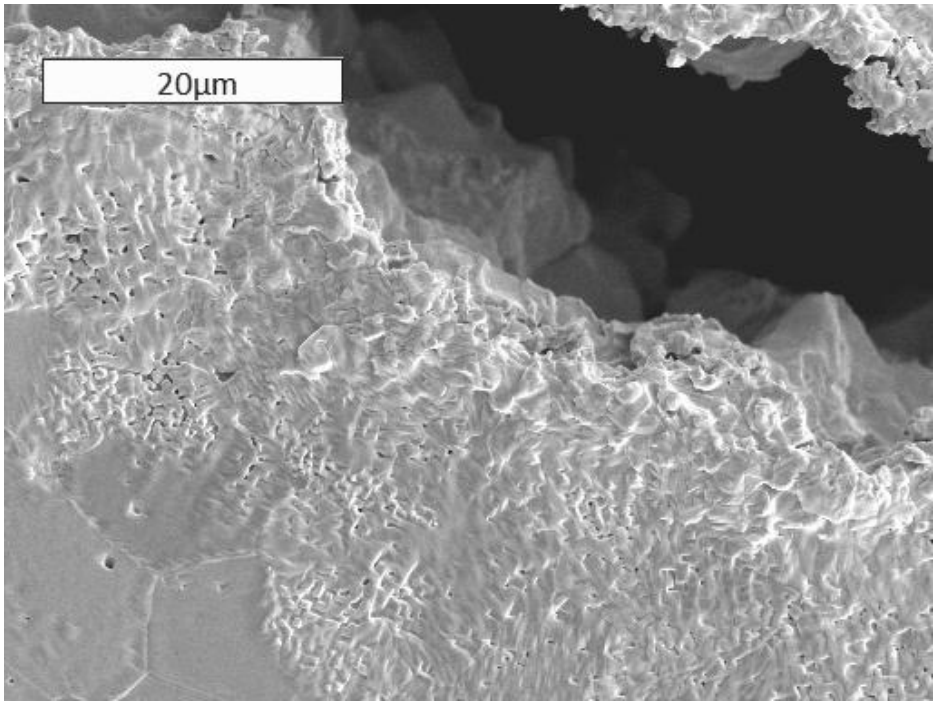


Figure 4-4. TaC SE image showing fracture zone

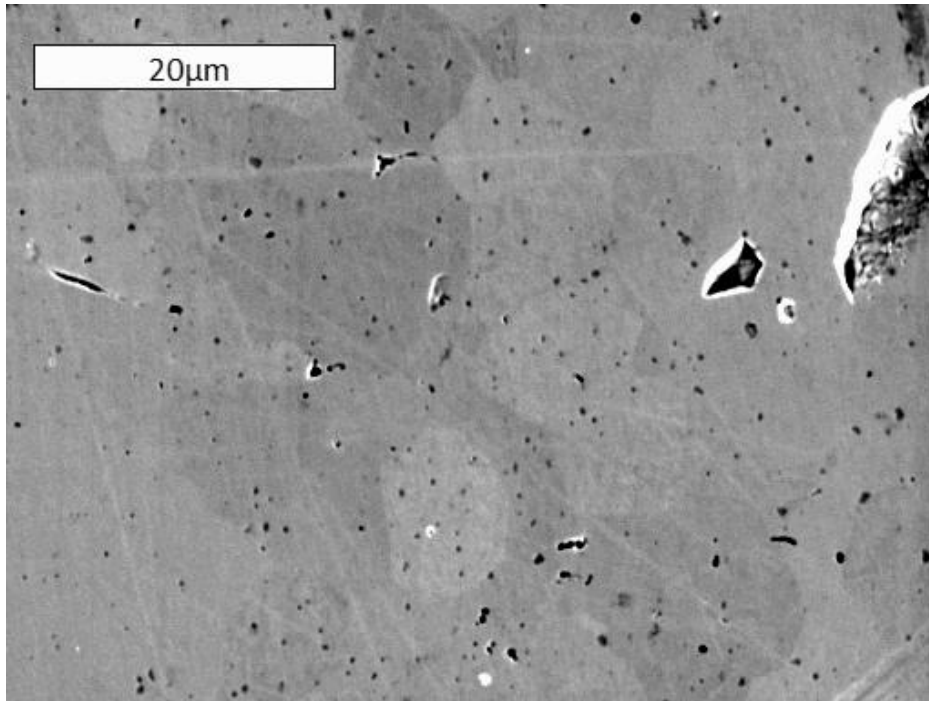


Figure 4-5. TaC SE image of pre-HHT specimen

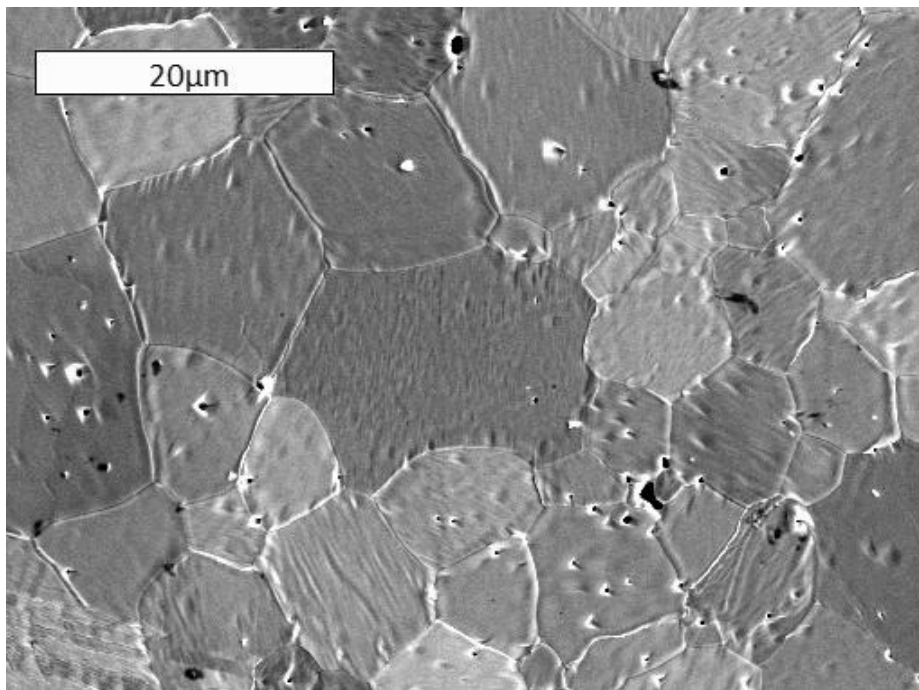


Figure 4-6. TaC SE image of post-HHT specimen

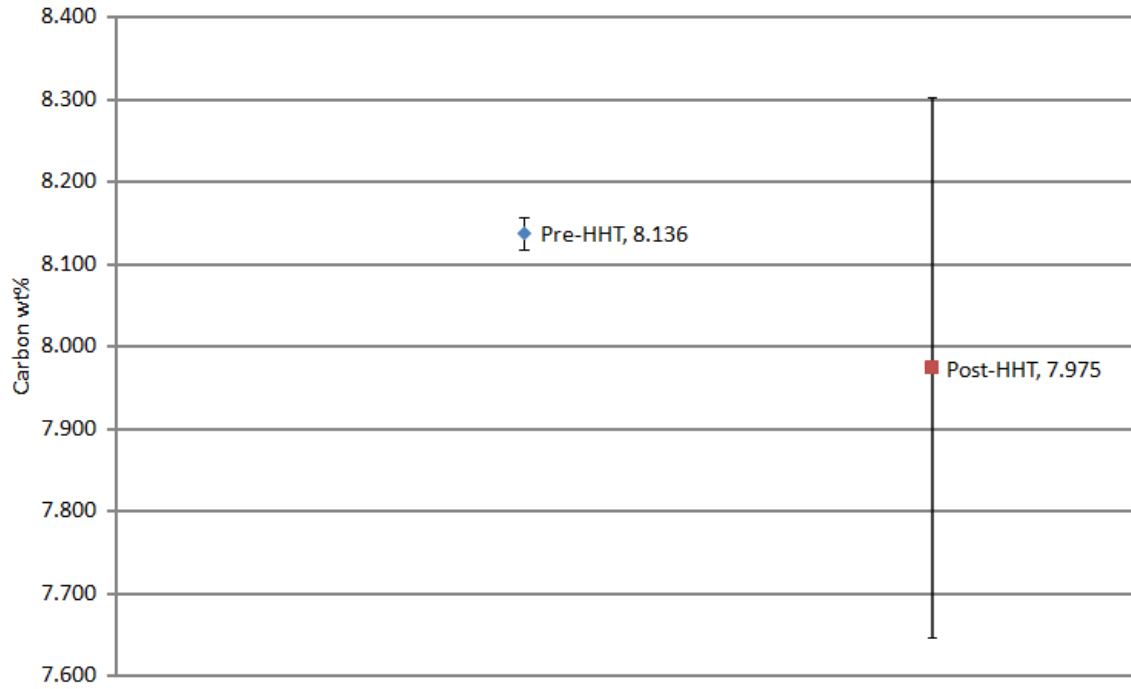


Figure 4-7. TaC bulk carbon content

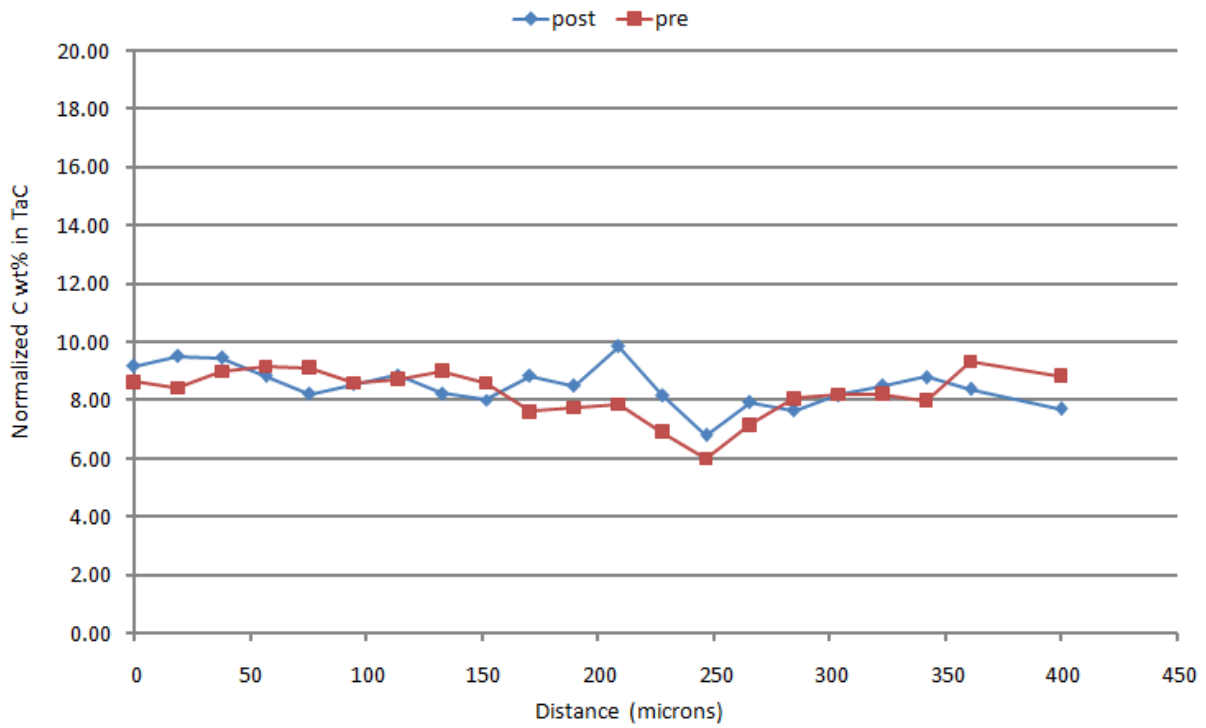


Figure 4-8. Mid-axial cross section showing TaC carbon content as a function of depth

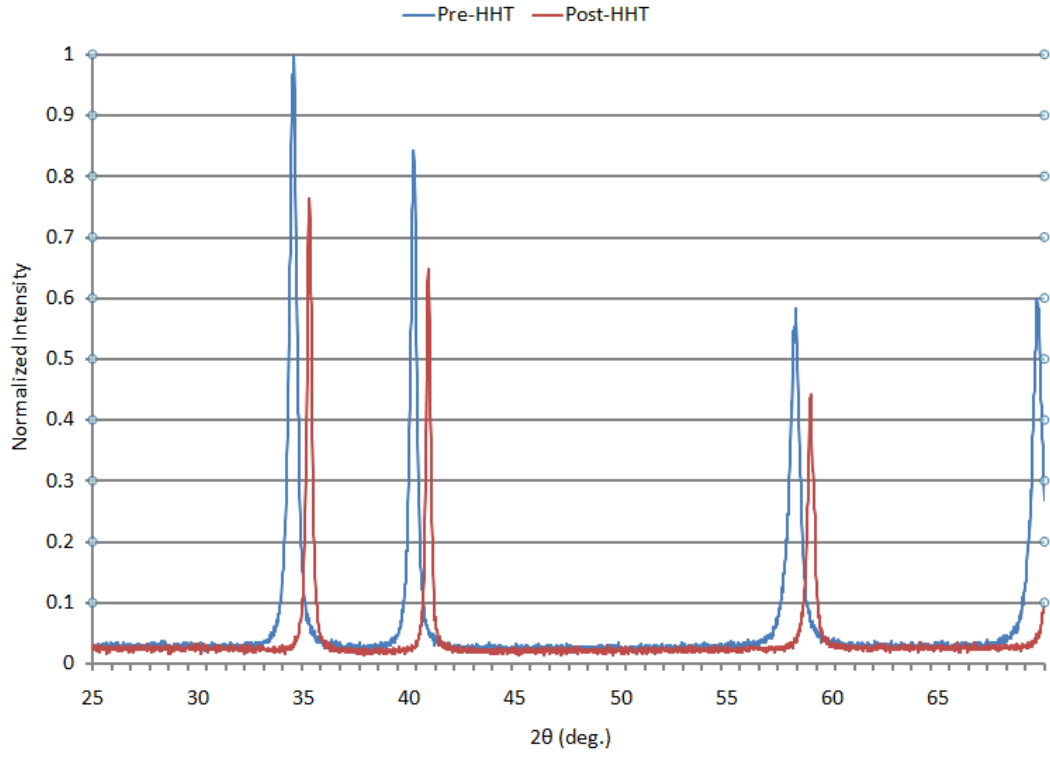


Figure 4-9. TaC pre- and post-HHT XRD spectrum

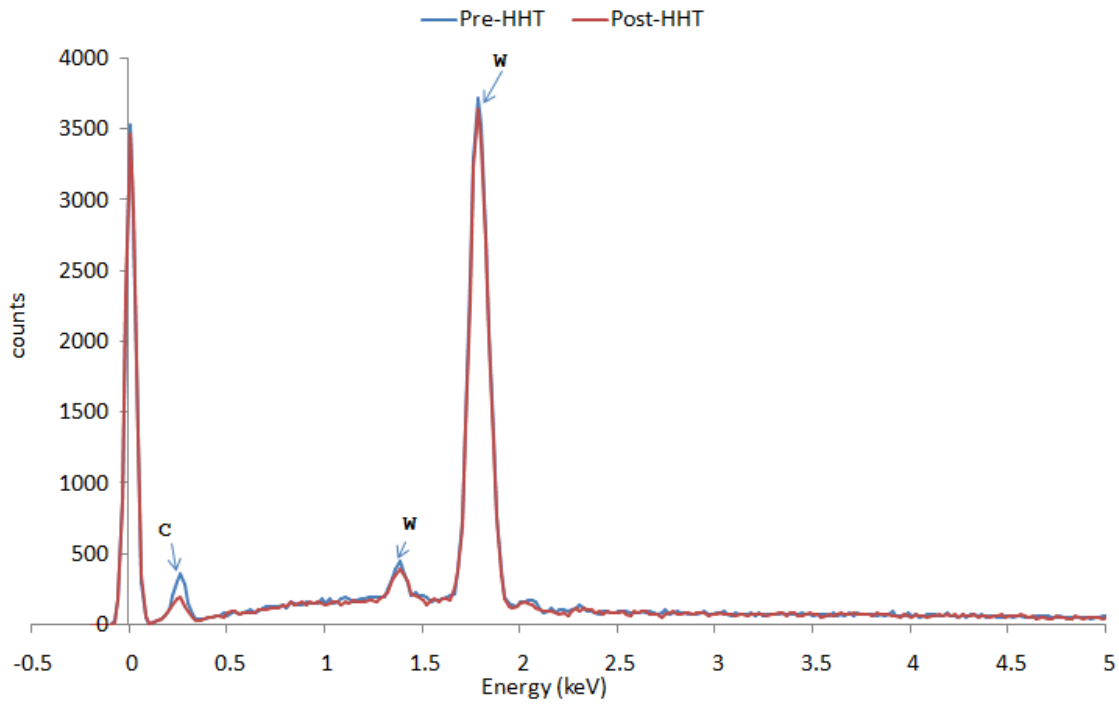


Figure 4-10. EDS of pre- and post-HHT of WC sample

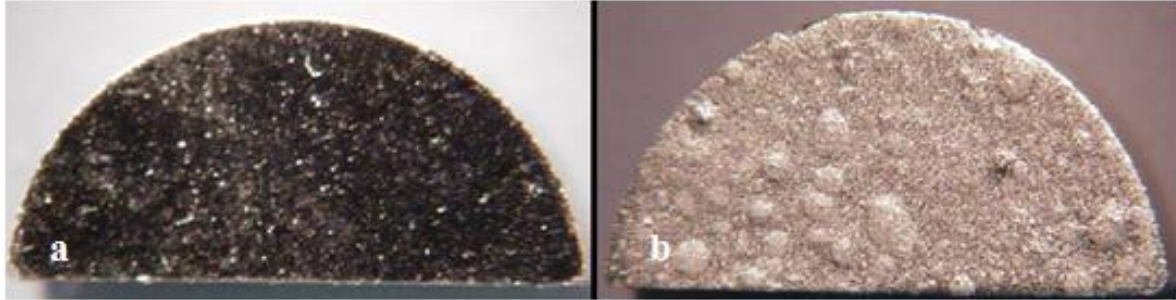


Figure 4-11. Optical image of WC. A) Pre-HHT WC sample. B) Post-HHT WC sample

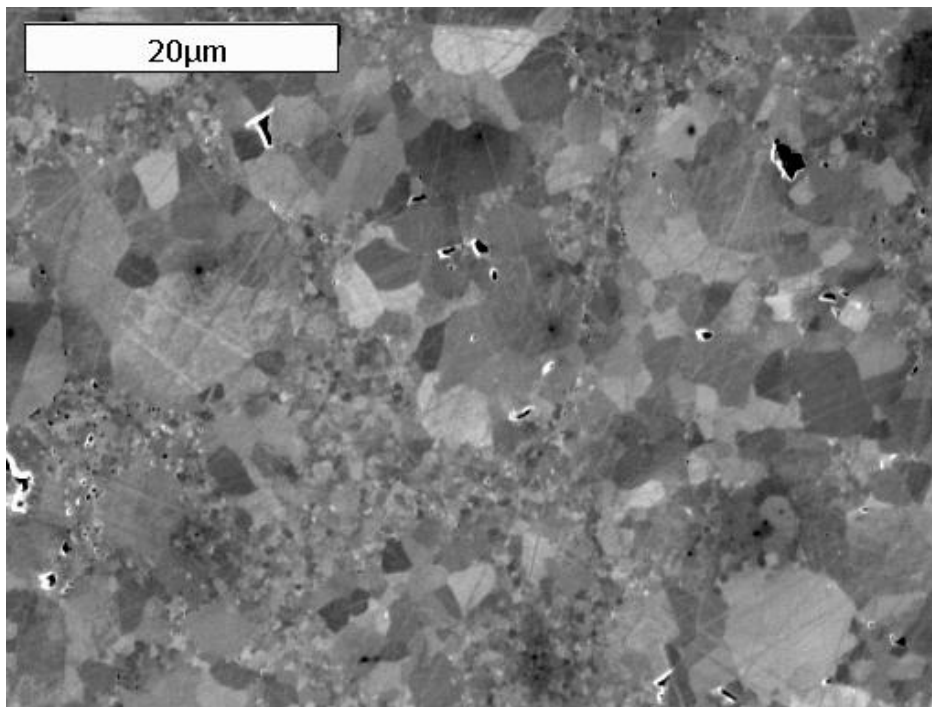


Figure 4-12. WC SE image of pre-HHT specimen

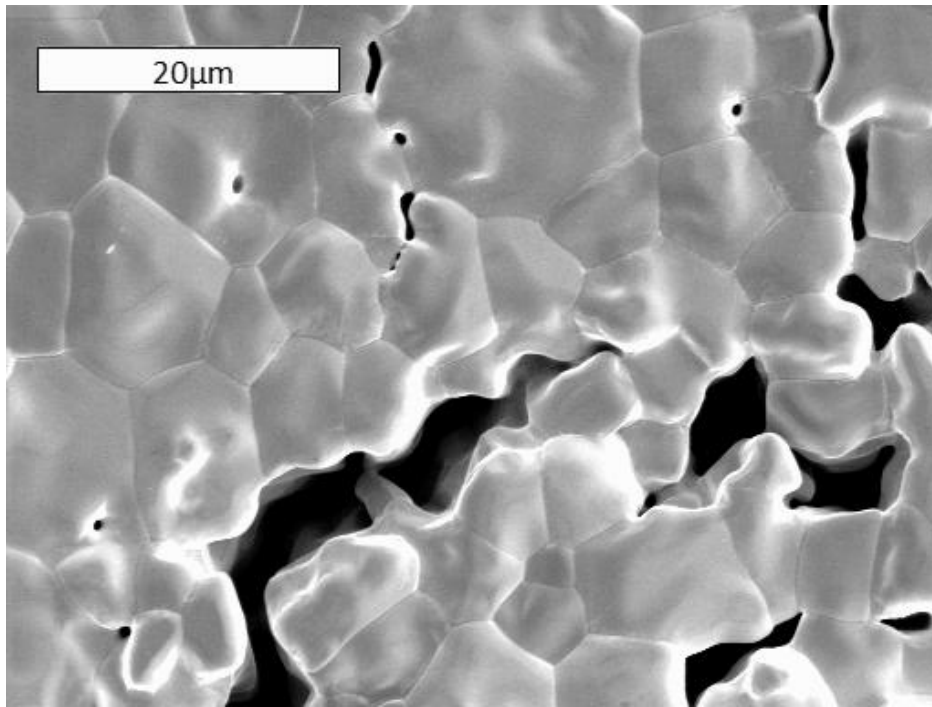


Figure 4-13. WC SE image of post-HHT specimen

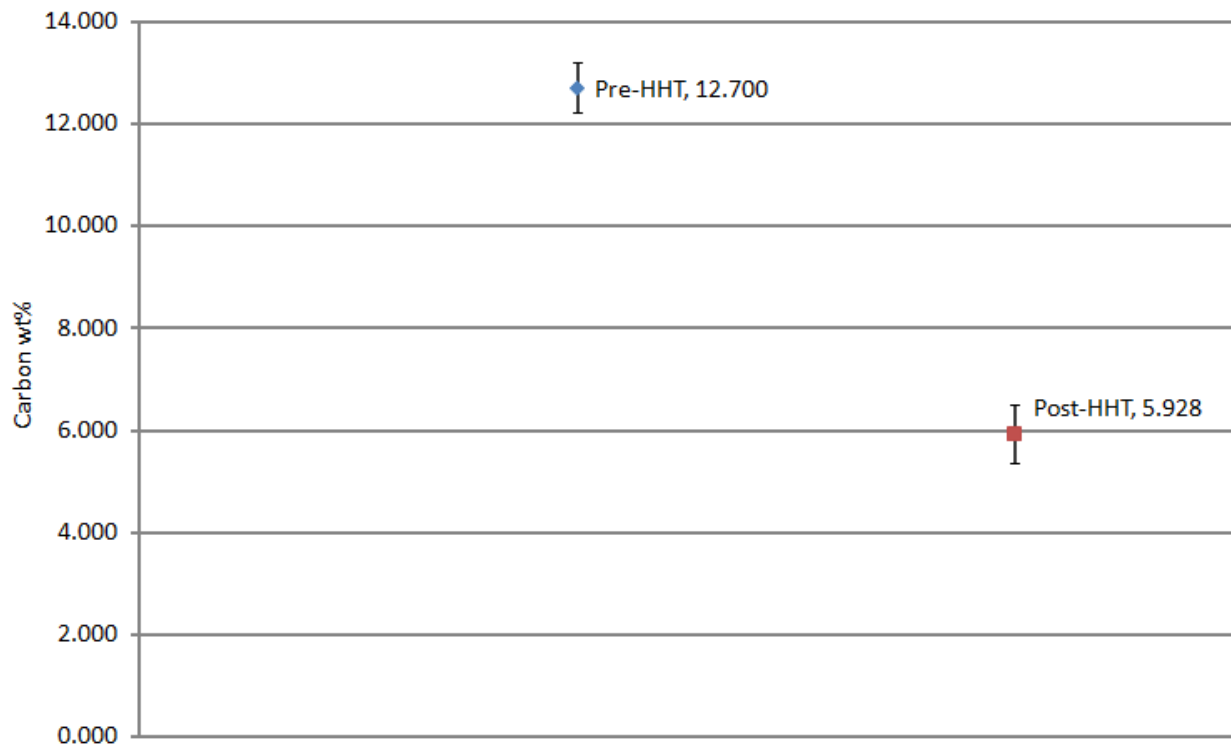


Figure 4-14. WC bulk carbon content

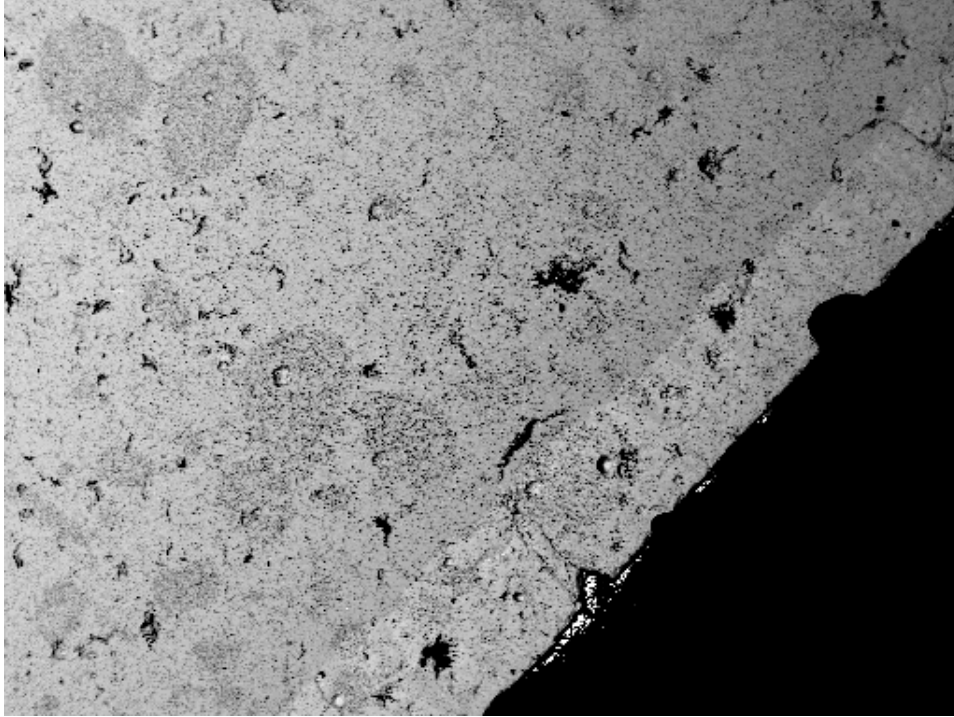


Figure 4-15. WC BSE image showing the transition zone where carbon depletion occurred

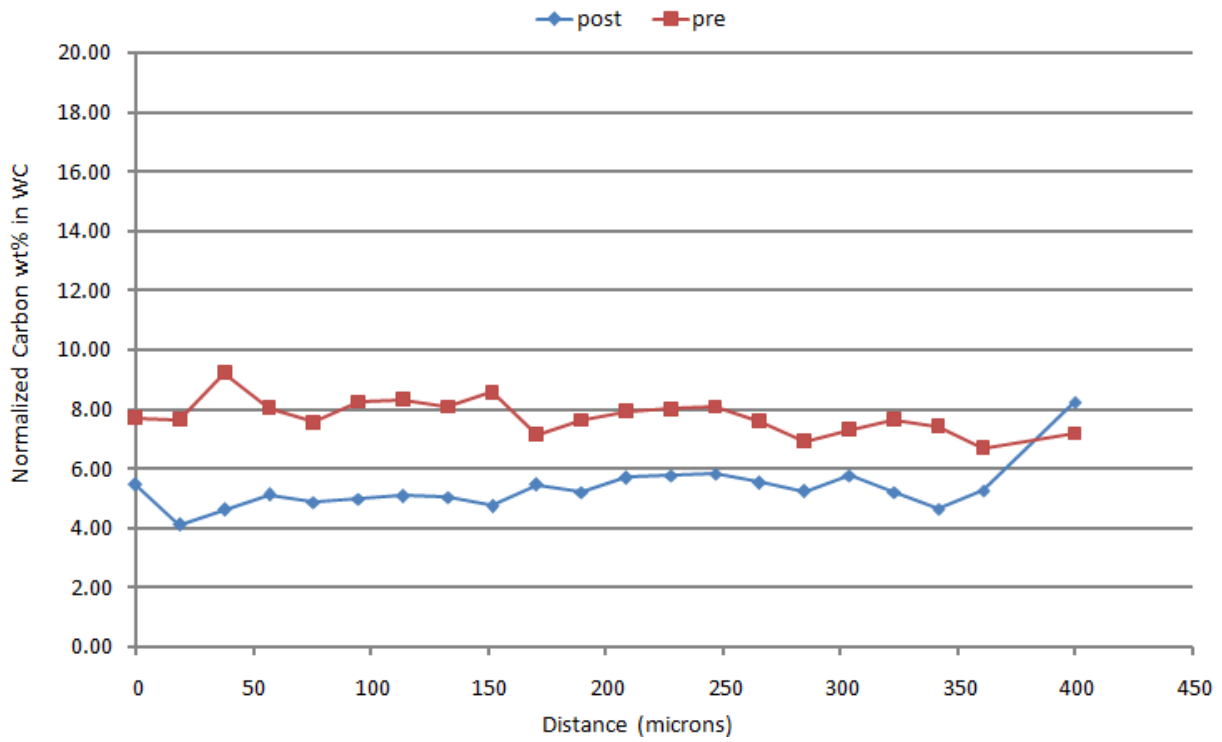


Figure 4-16. Mid-axial cross section showing WC carbon content as a function of depth

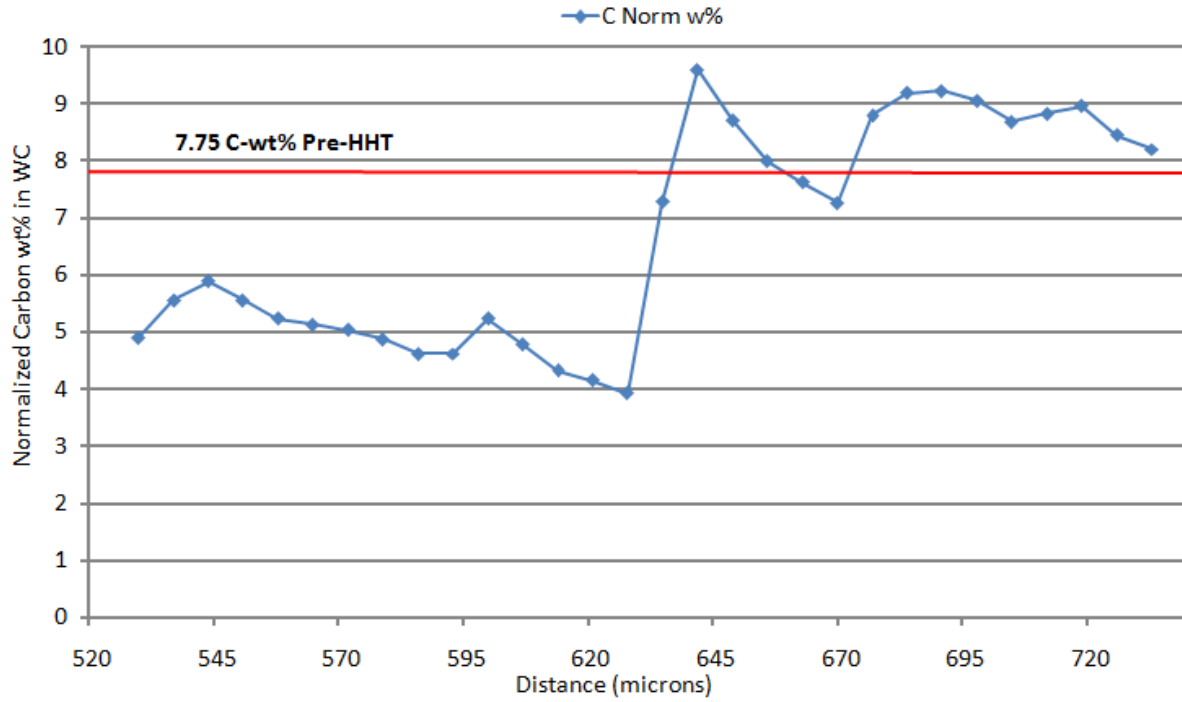


Figure 4-17. Mid-axial cross section of post-HHT showing WC transition zone of carbon content

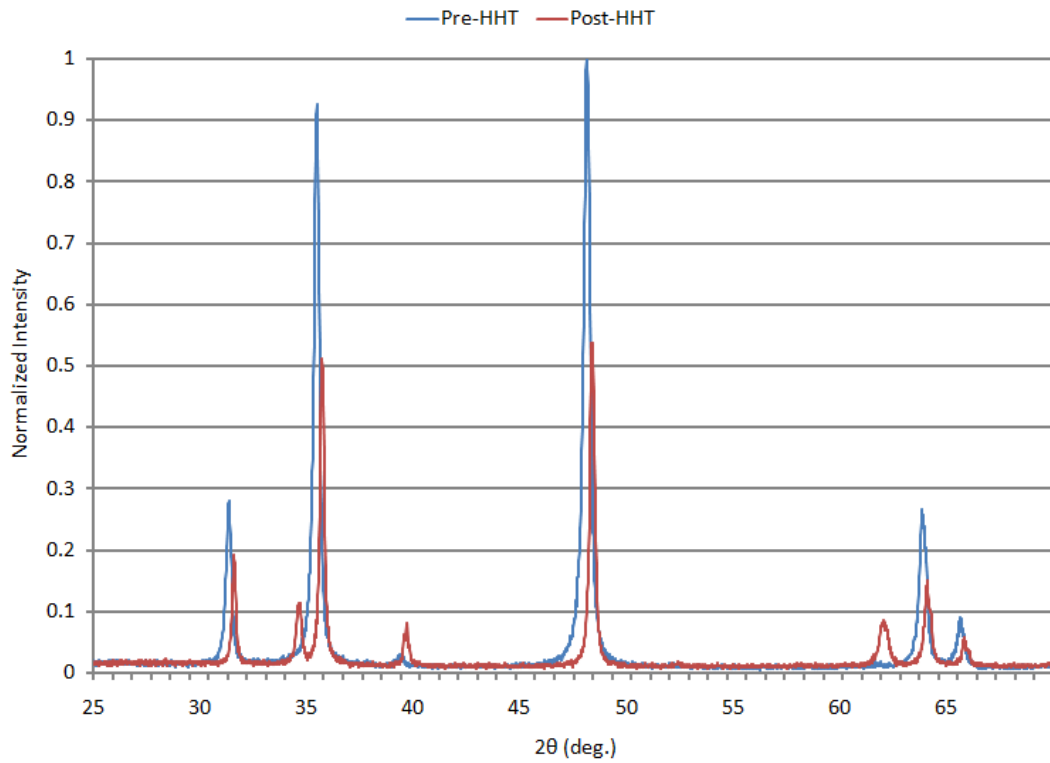


Figure 4-18. WC pre- and post-HHT XRD spectrum

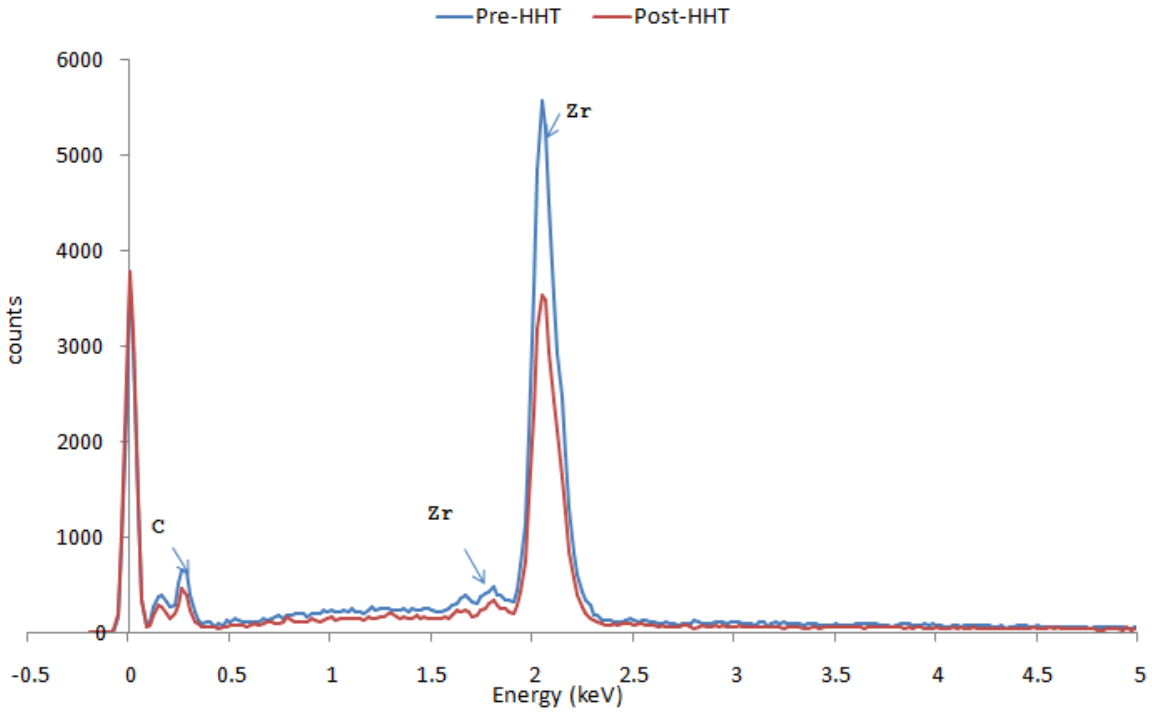


Figure 4-19. EDS of pre- and post-HHT of ZrC sample

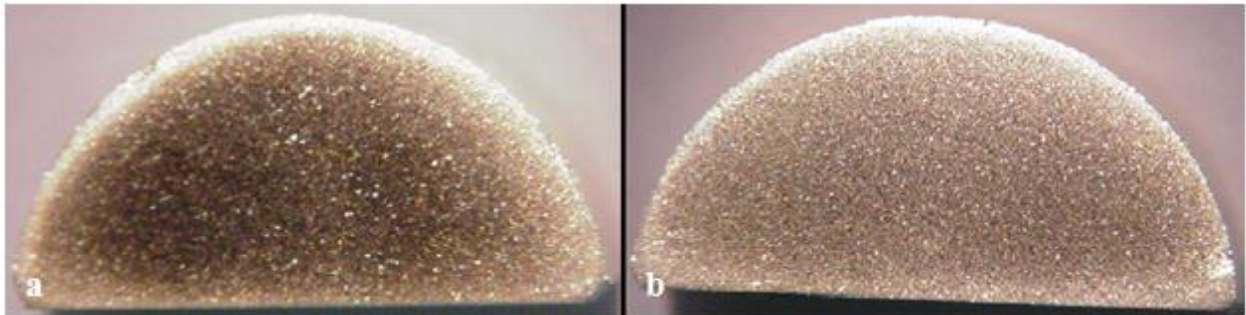


Figure 4-20. Optical image of ZrC. A) Pre-HHT ZrC sample. B) Post-HHT ZrC sample.

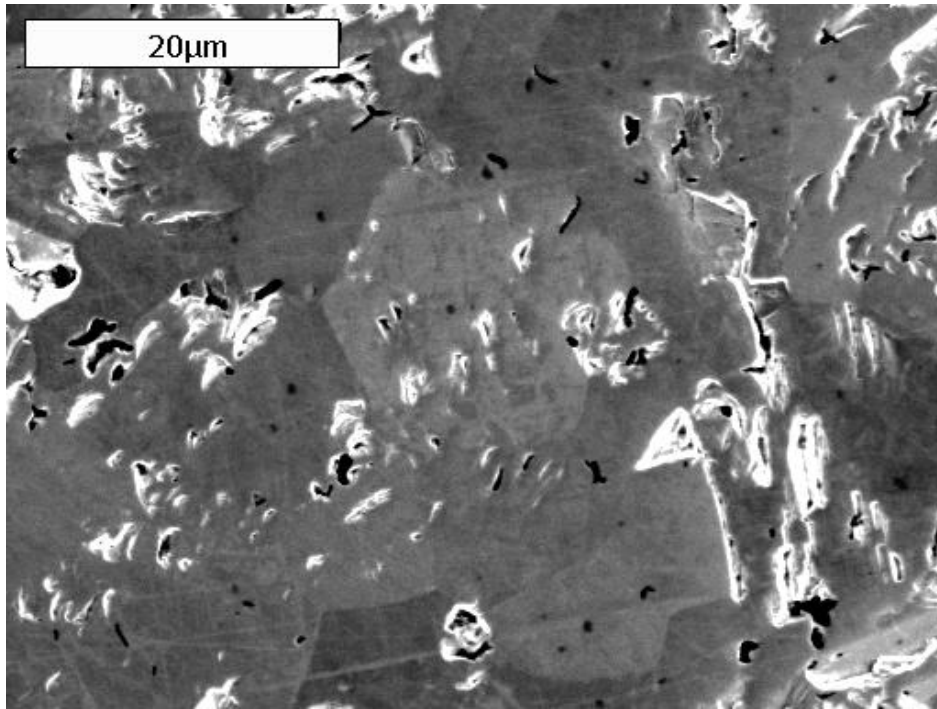


Figure 4-21. ZrC SE image of pre-HHT specimen

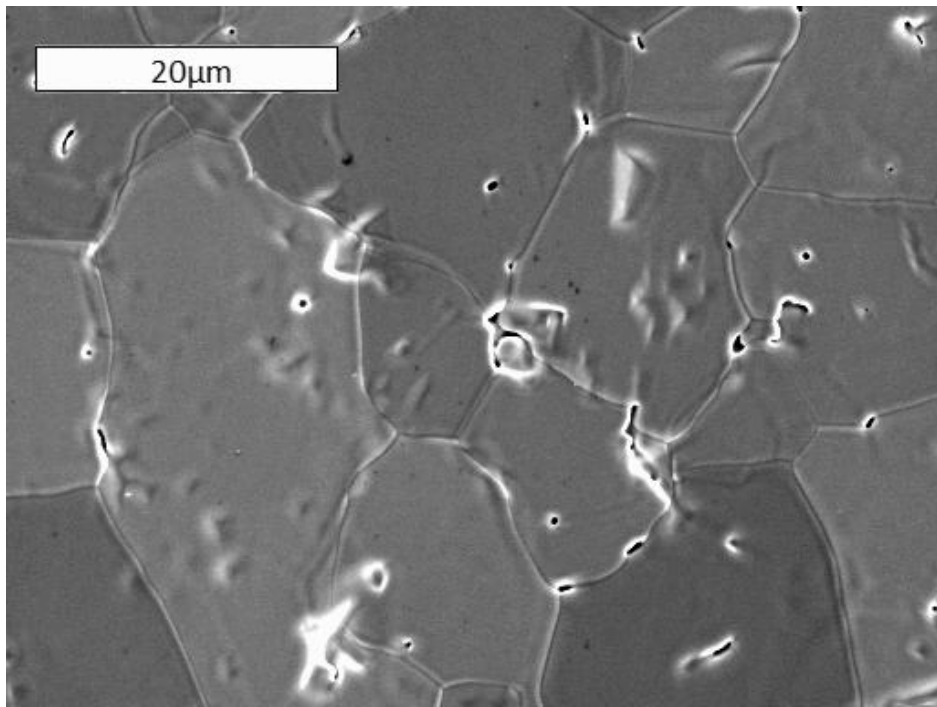


Figure 4-22. ZrC SE image of post-HHT specimen

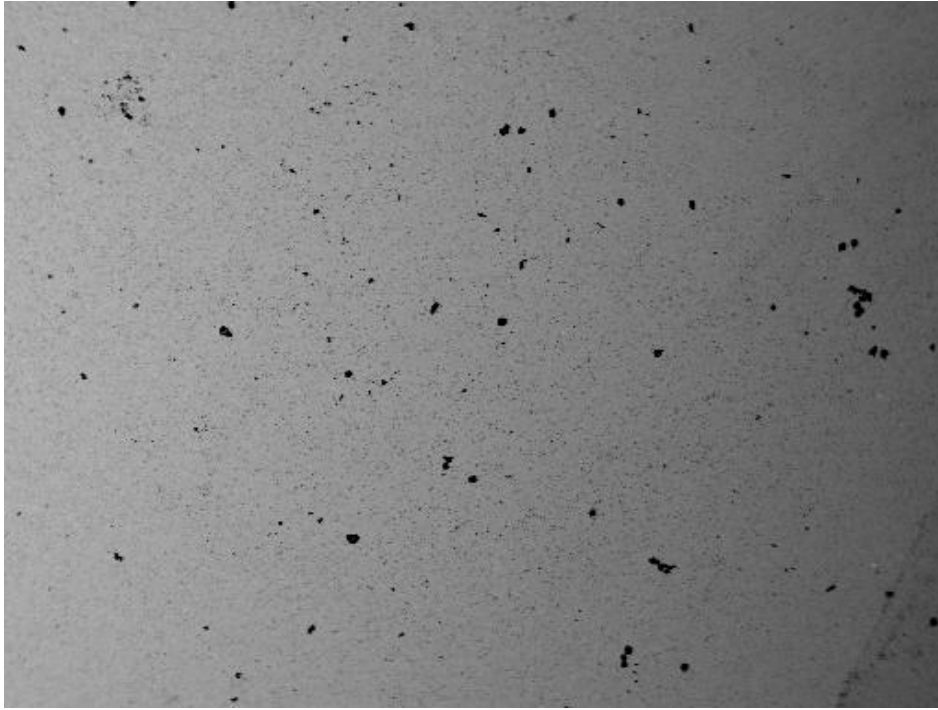


Figure 4-23. ZrC BSE image of pre-HHT specimen

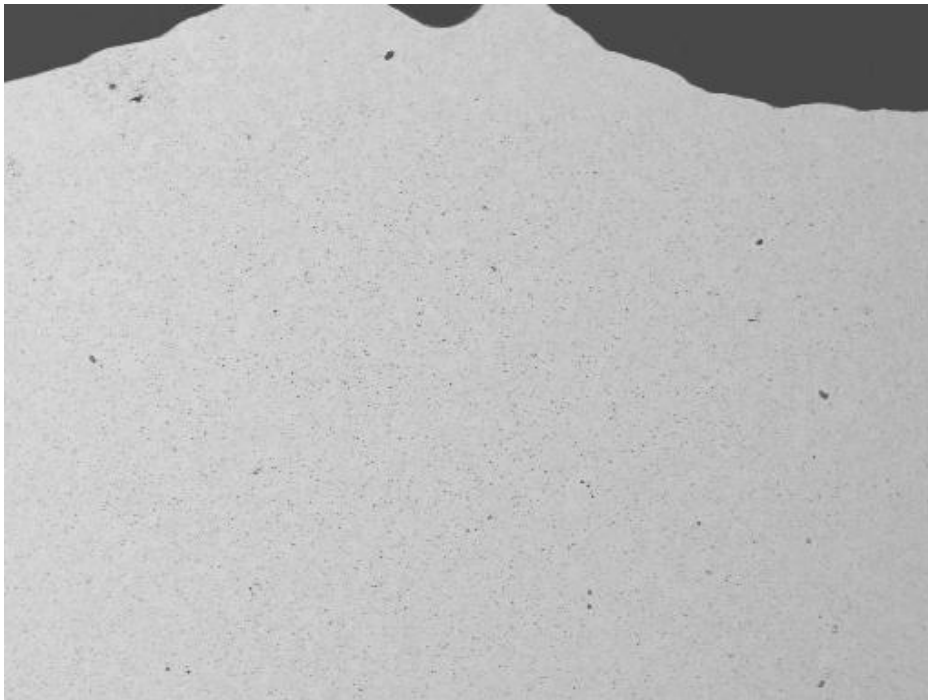


Figure 4-24. ZrC BSE image of post-HHT specimen

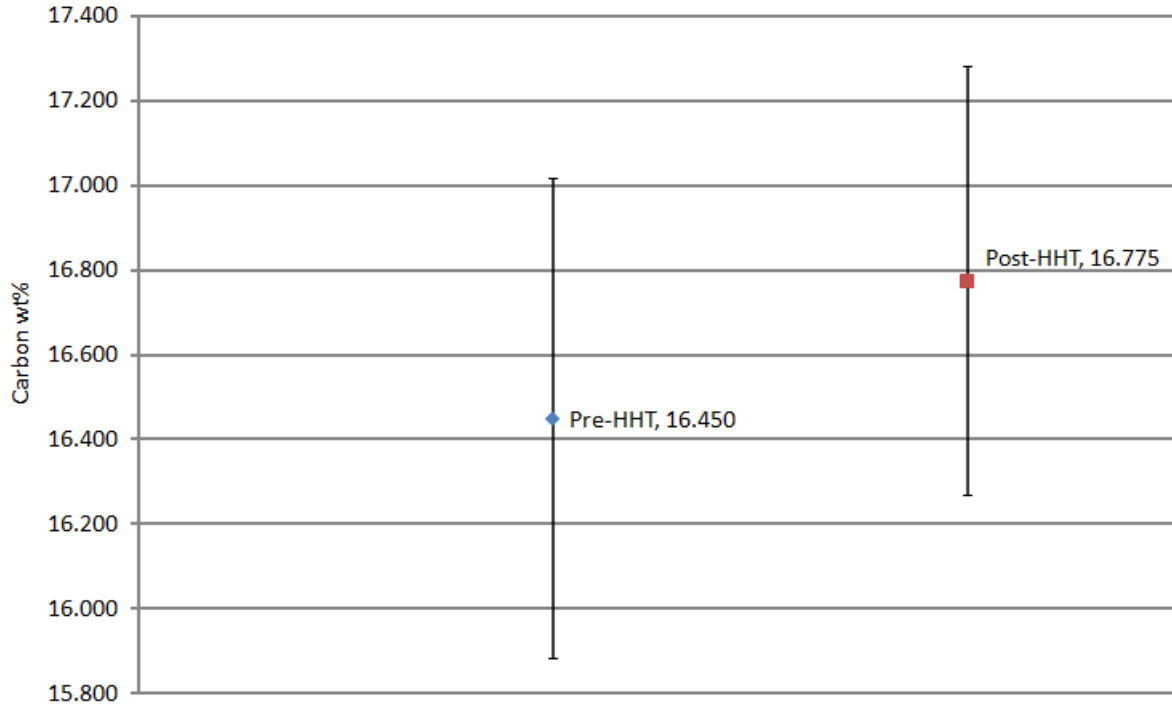


Figure 4-25. ZrC bulk carbon content.

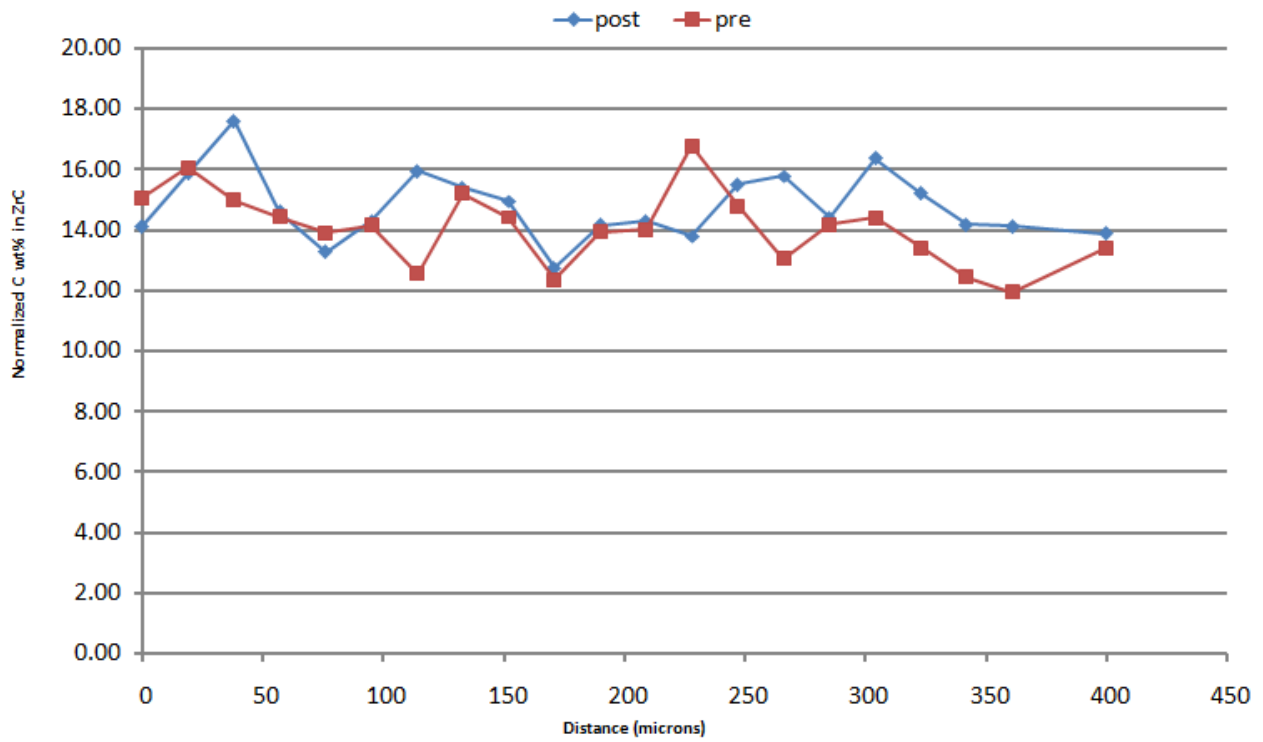


Figure 4-26. Mid-axial cross section showing ZrC carbon content as a function of depth.

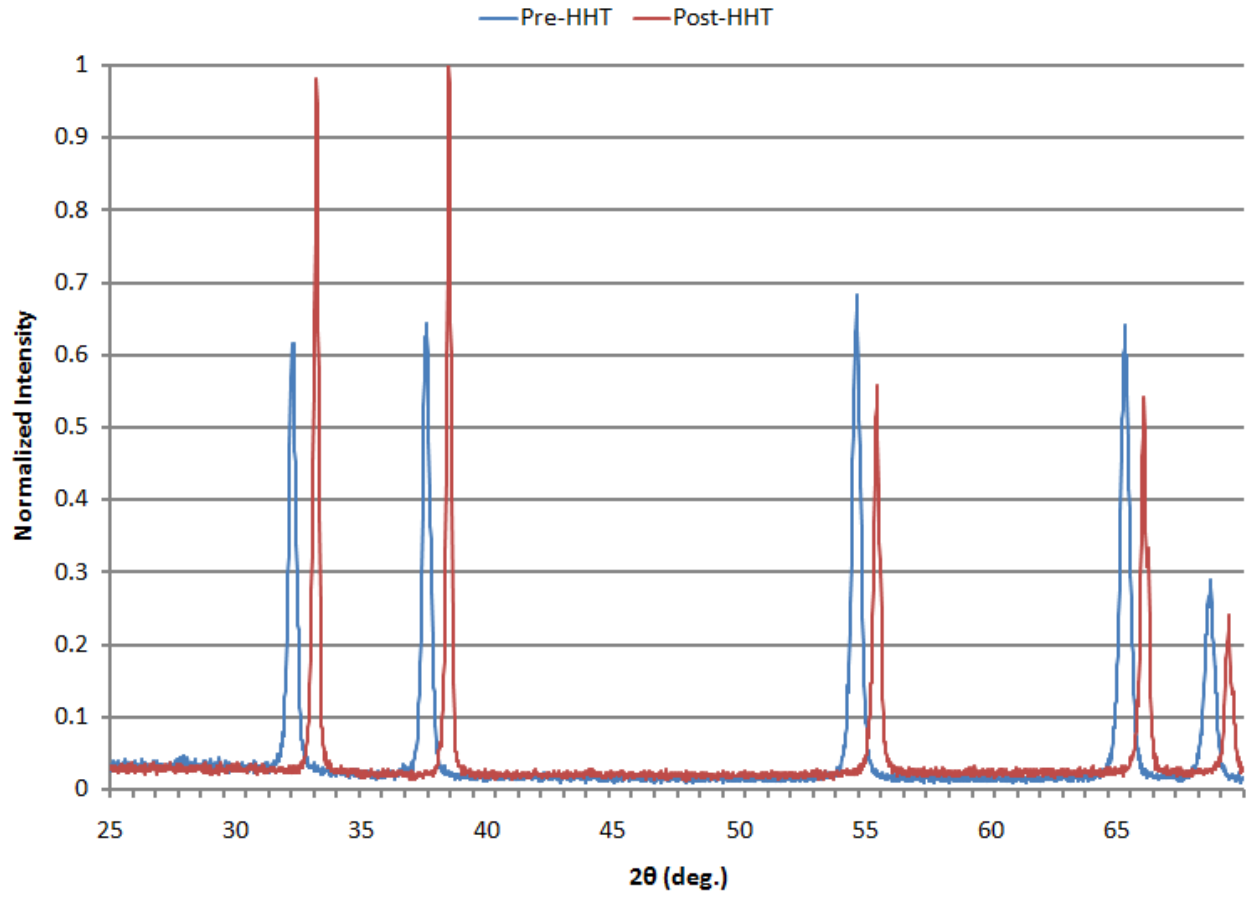


Figure 4-27. ZrC pre- and post-HHT XRD spectrum

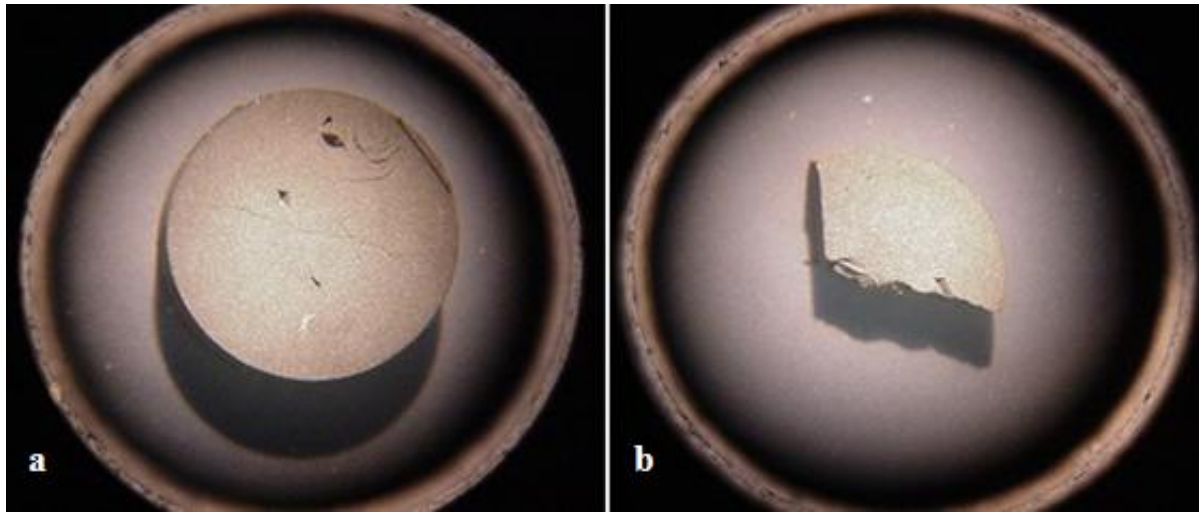


Figure 4-28. Optical image of TRI-C1. A) TRI-C1 pre-HHT. B) TRI-C1 post-HHT

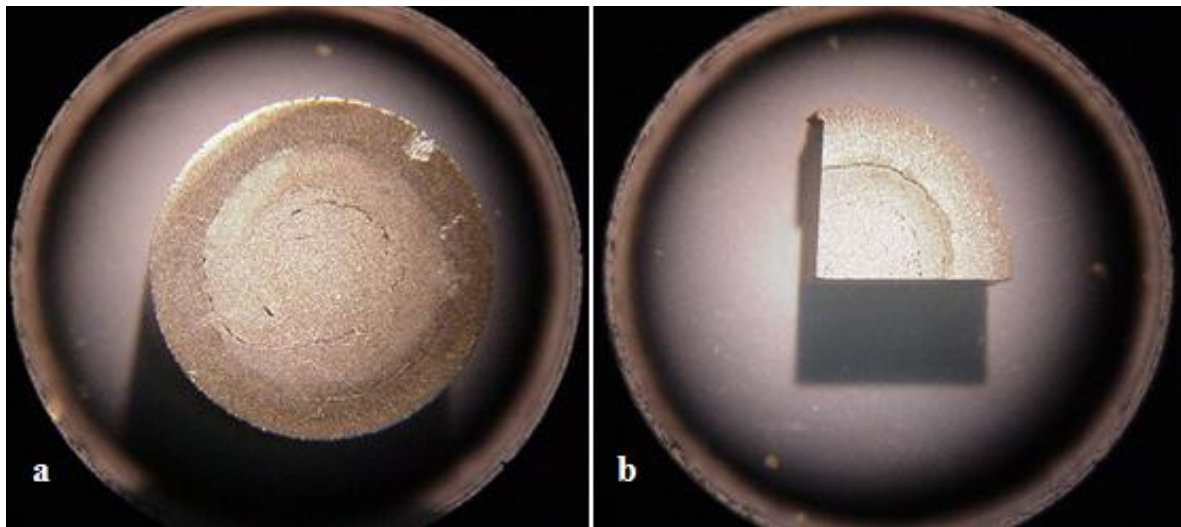


Figure 4-29. Optical image of TRI-C2. A) TRI-C2 pre-HHT. B) TRI-C2 post-HHT

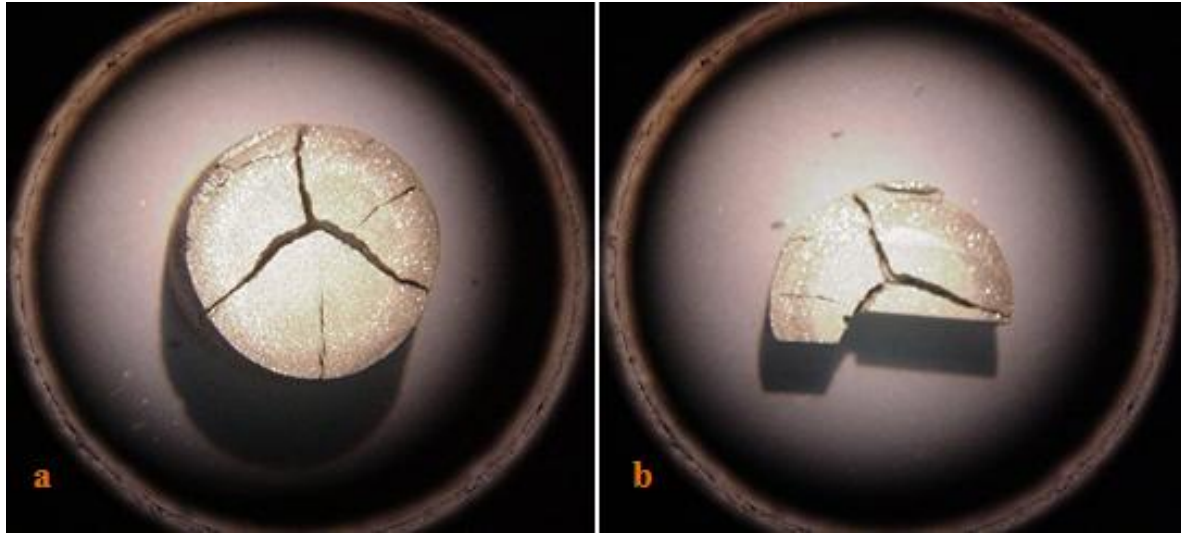


Figure 4-30. Optical image of TRI-C3. A) TRI-C3 pre-HHT. B) TRI-C3 post-HHT

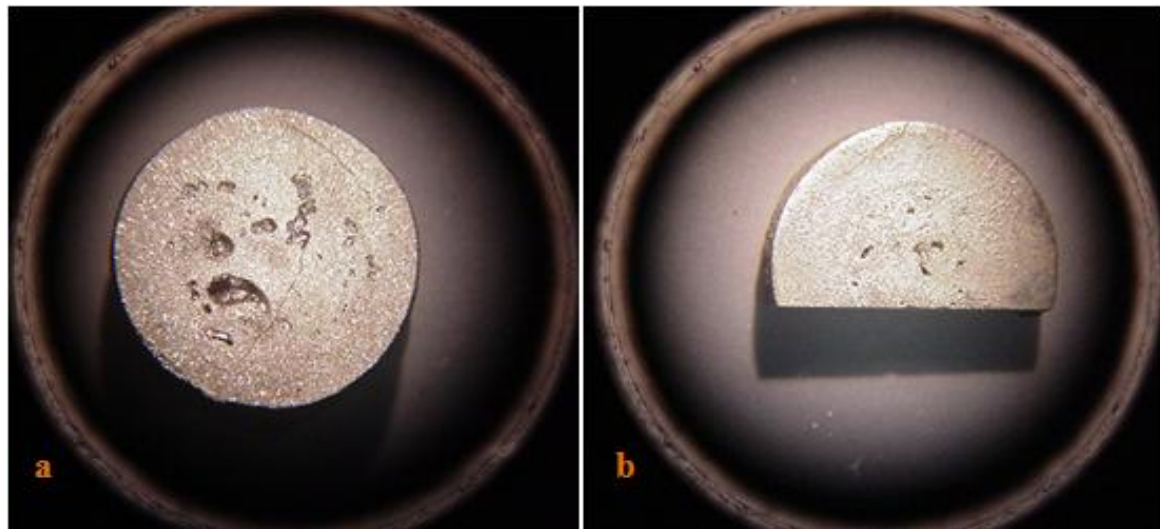


Figure 4-31. Optical image of TRI-C4. A) TRI-C4 pre-HHT. B) TRI-C4 post-HHT

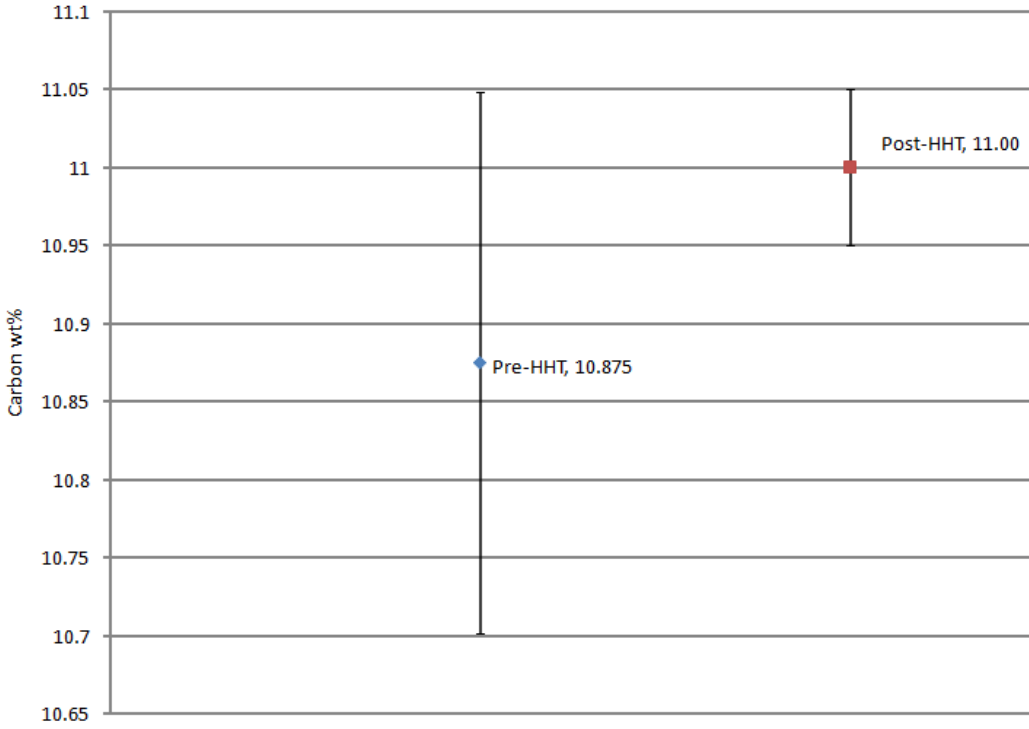


Figure 4-32. TRI-C1 pre- and post-HHT bulk carbon content

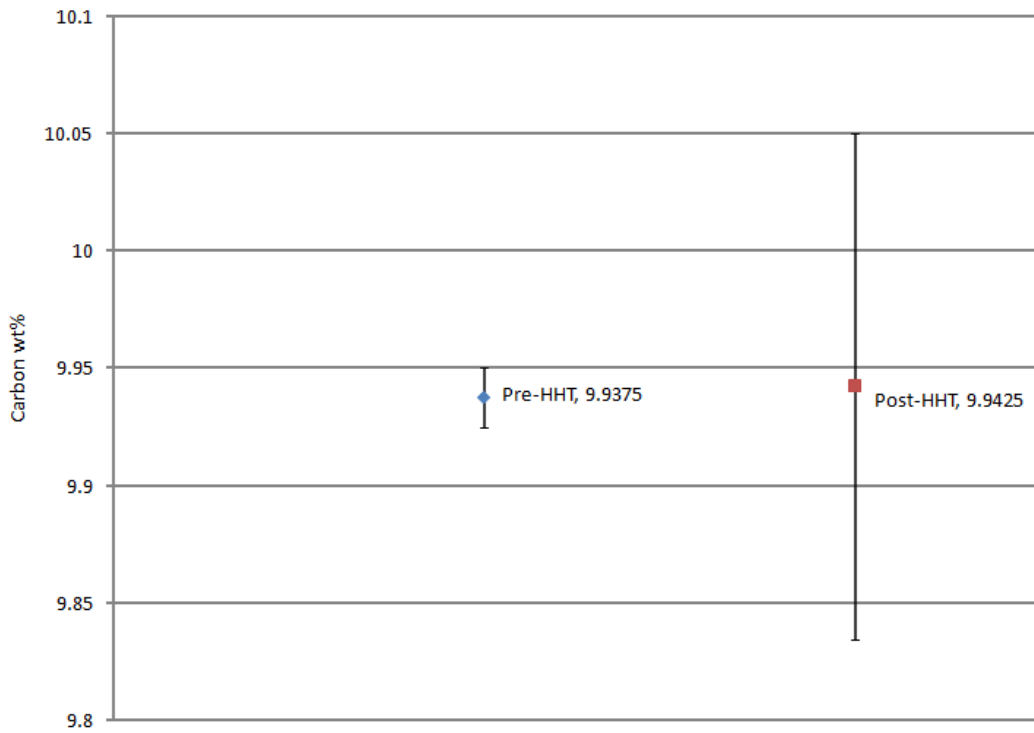


Figure 4-33. TRI-C2 pre- and post-HHT bulk carbon content

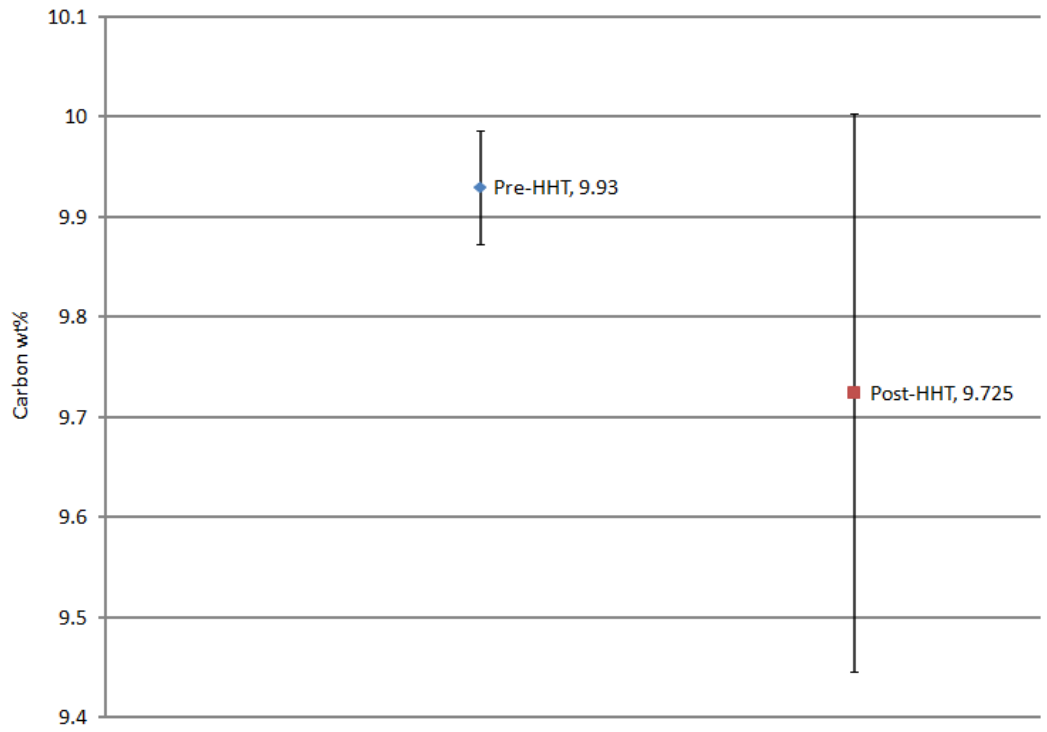


Figure 4-34. TRI-C3 pre- and post-HHT bulk carbon content

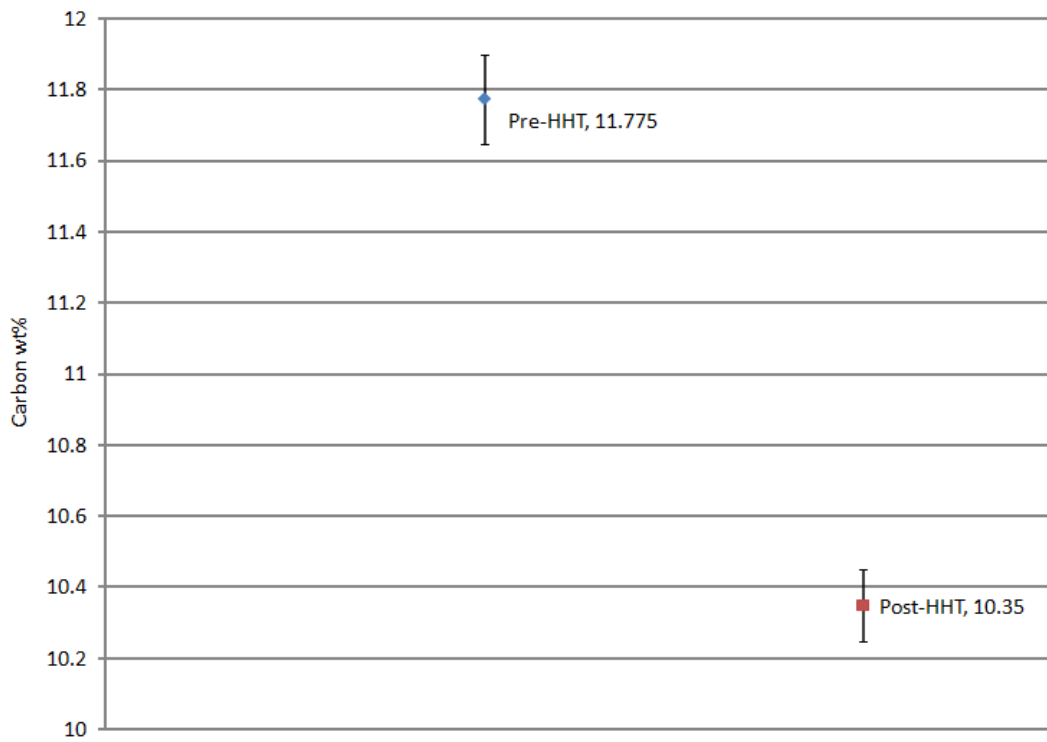


Figure 4-35. TRI-C4 pre- and post-HHT bulk carbon content

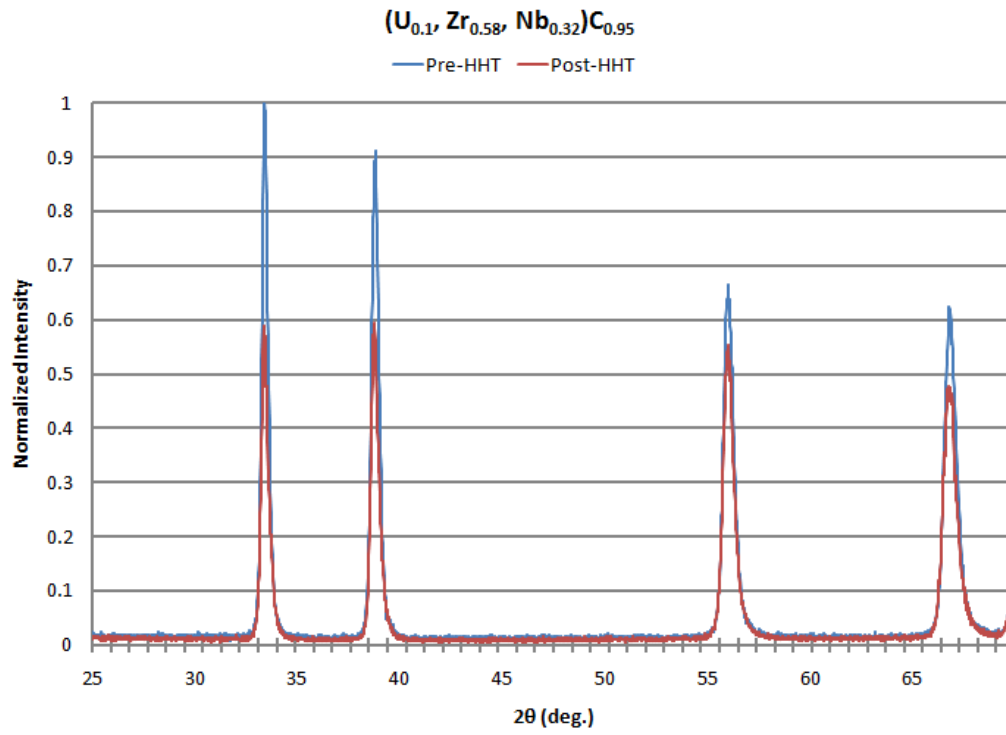


Figure 4-36. TRI-C1 XRD spectrum

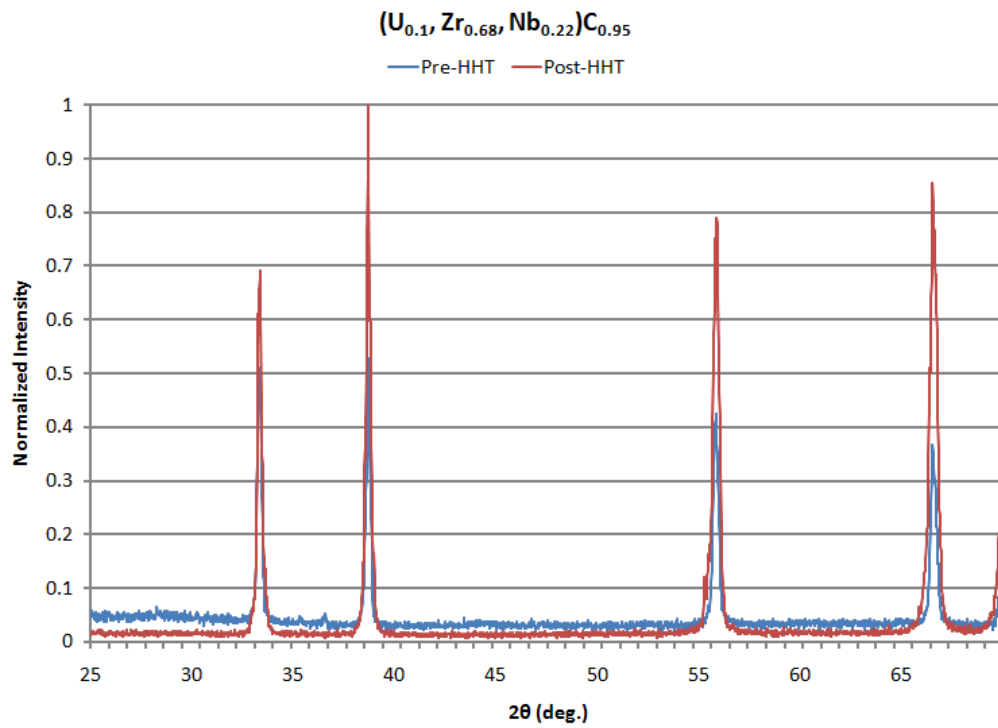


Figure 4-37. TRI-C2 XRD spectrum

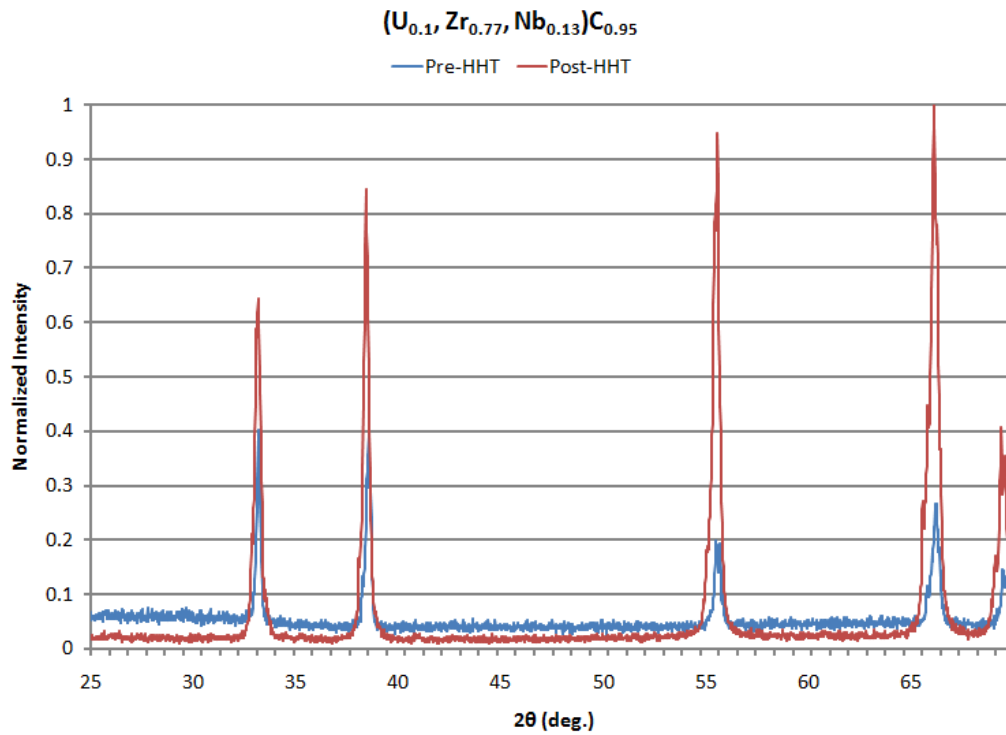


Figure 4-38. TRI-C3 XRD spectrum

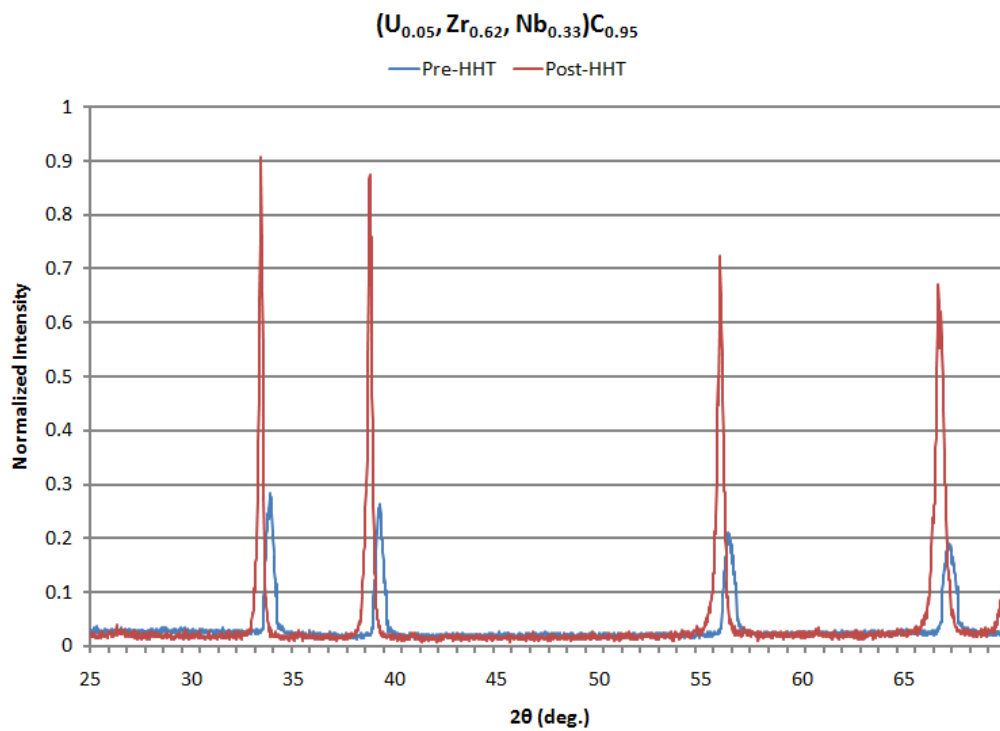


Figure 4-39. TRI-C4 XRD spectrum

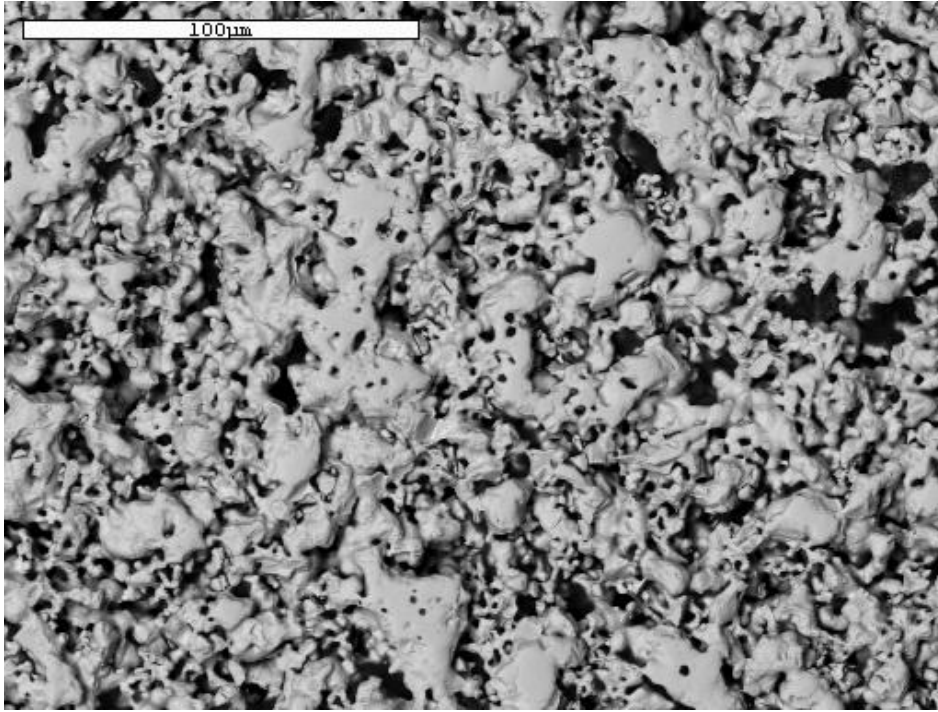


Figure 4-40. TRI-C1 BSE image of pre-HHT specimen

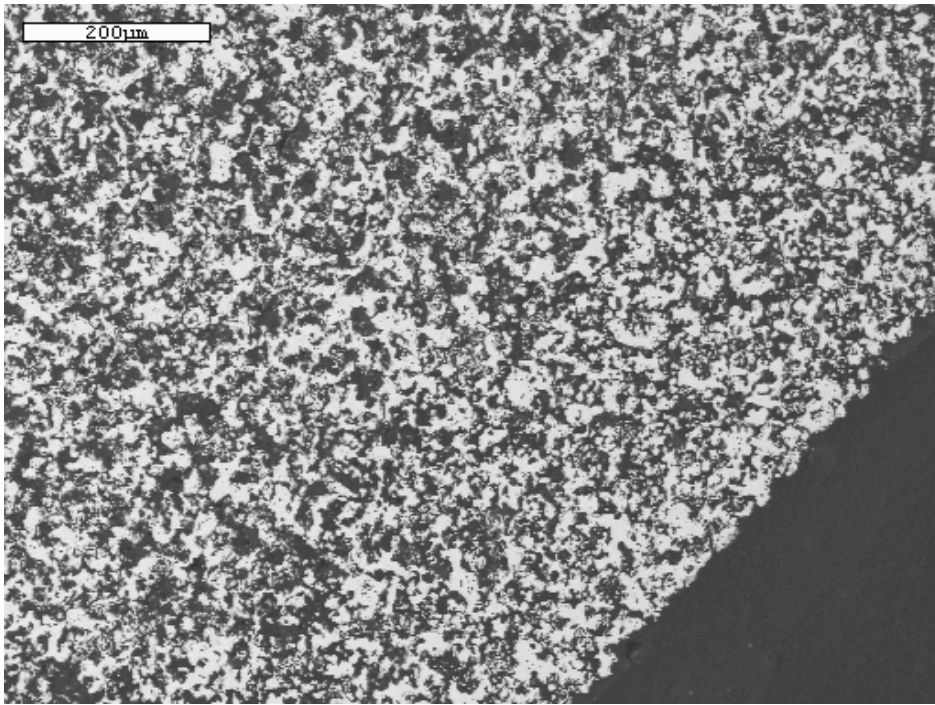


Figure 4-41. TRI-C1 BSE image of post-HHT specimen

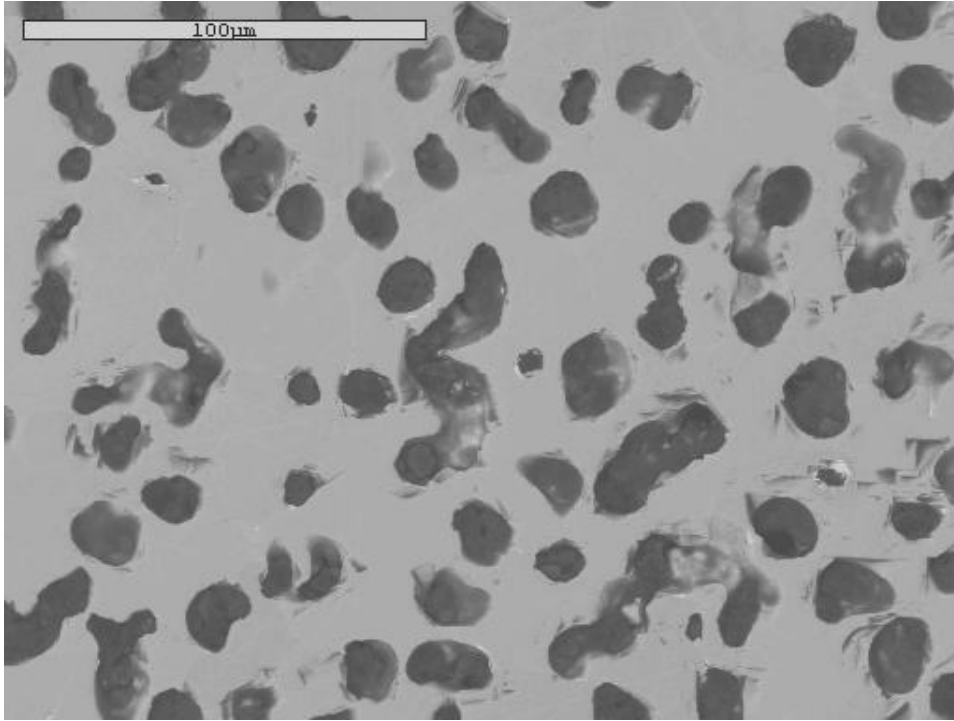


Figure 4-42. TRI-C2 BSE image of pre-HHT specimen

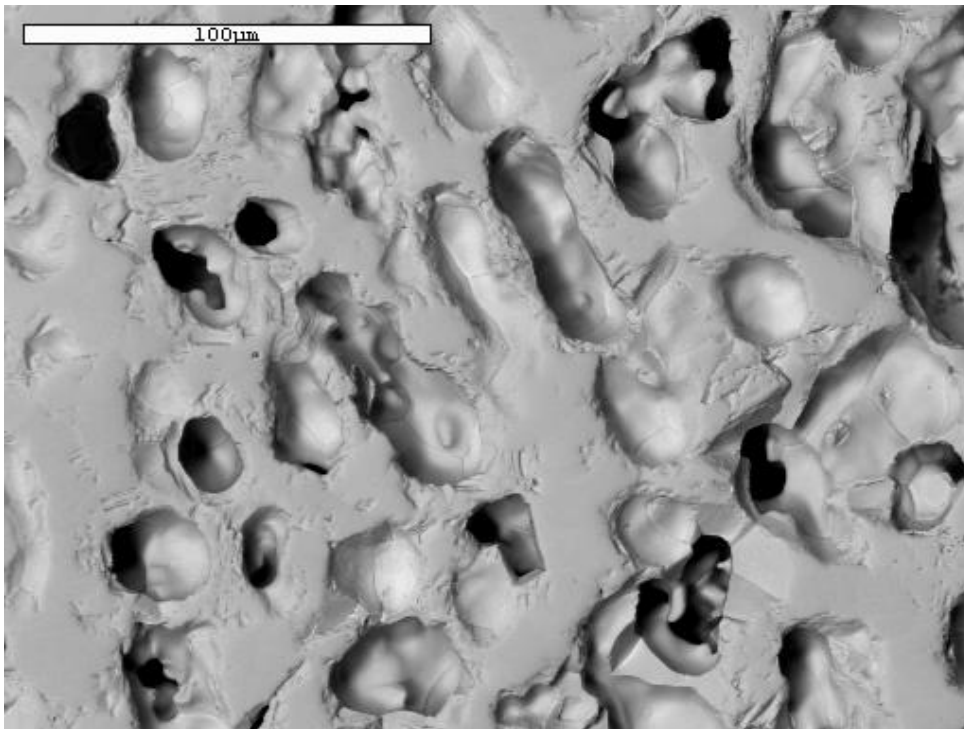


Figure 4-43. TRI-C2 BSE image of post-HHT specimen

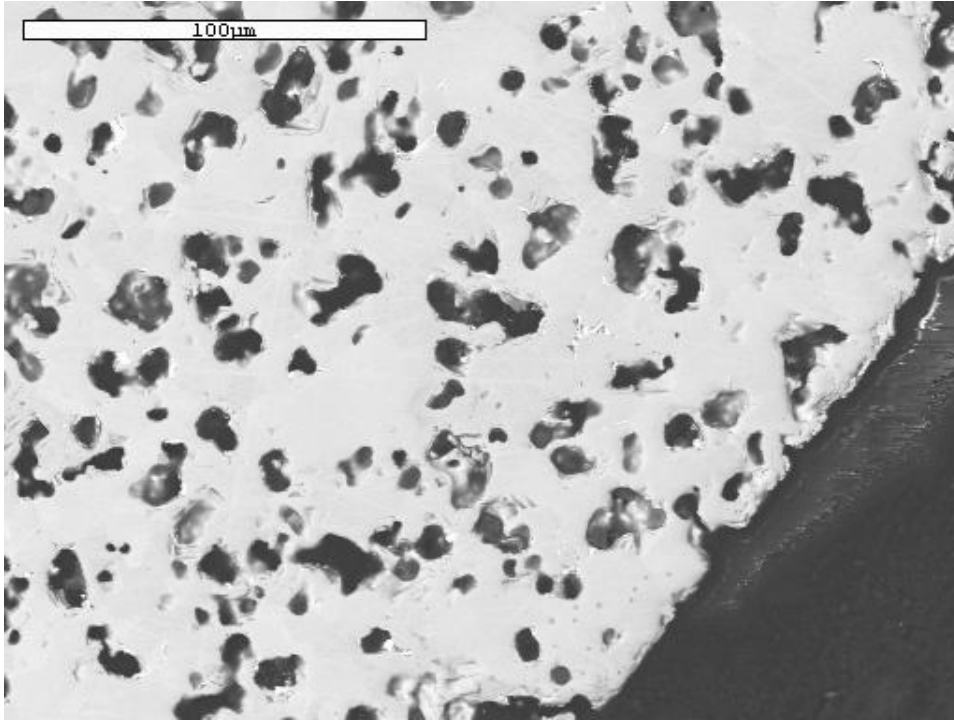


Figure 4-44. TRI-C3 BSE image of pre-HHT specimen

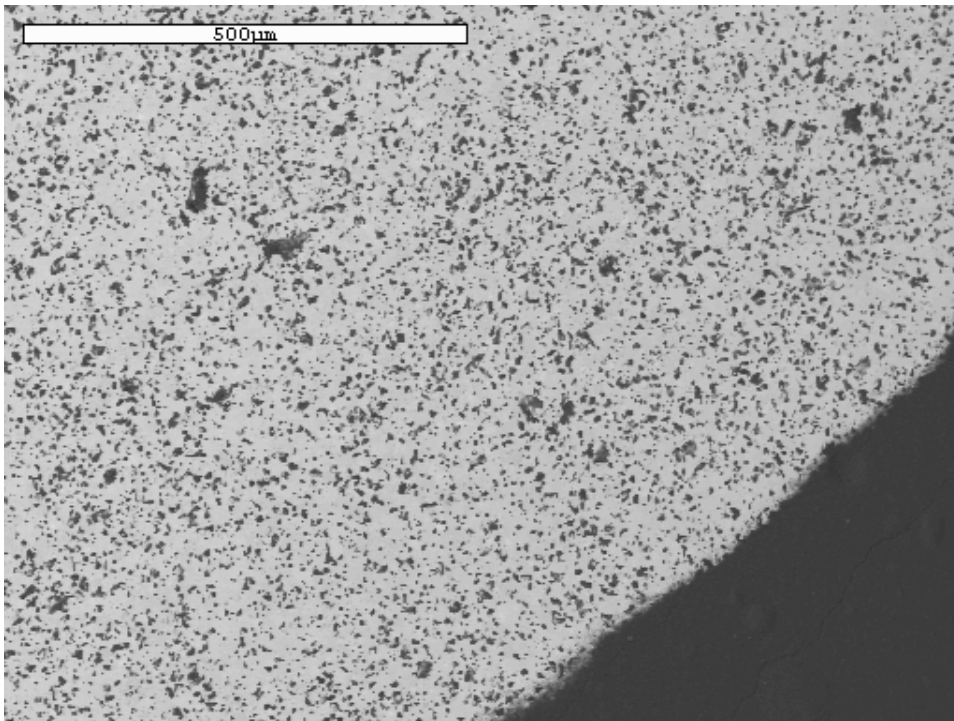


Figure 4-45. TRI-C3 SE image of post-HHT specimen

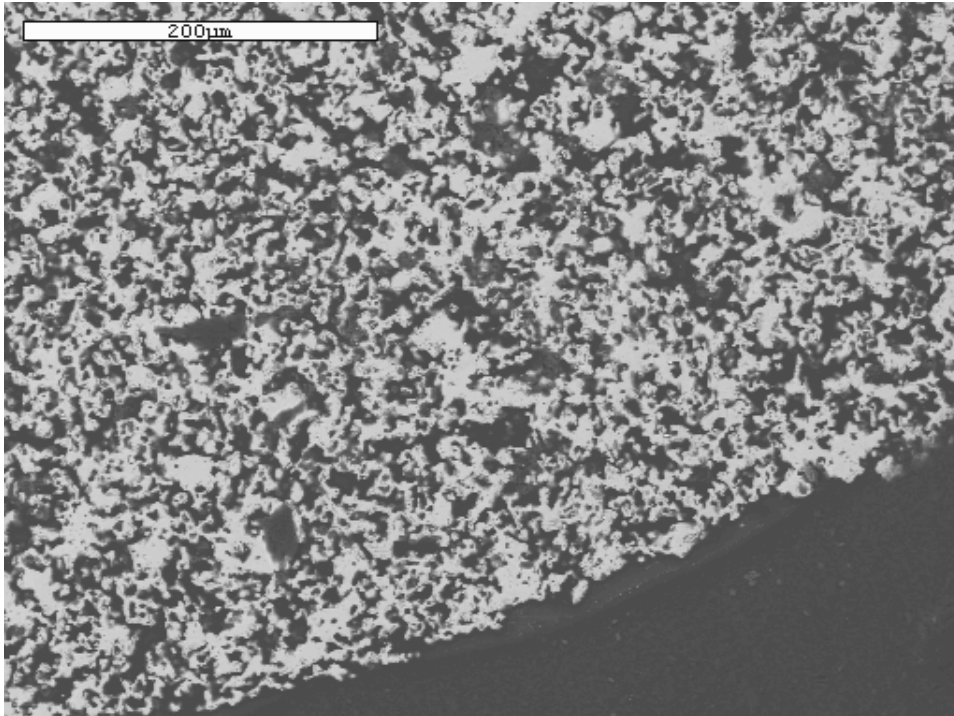


Figure 4-46. TRI-C4 BSE image of pre-HHT specimen

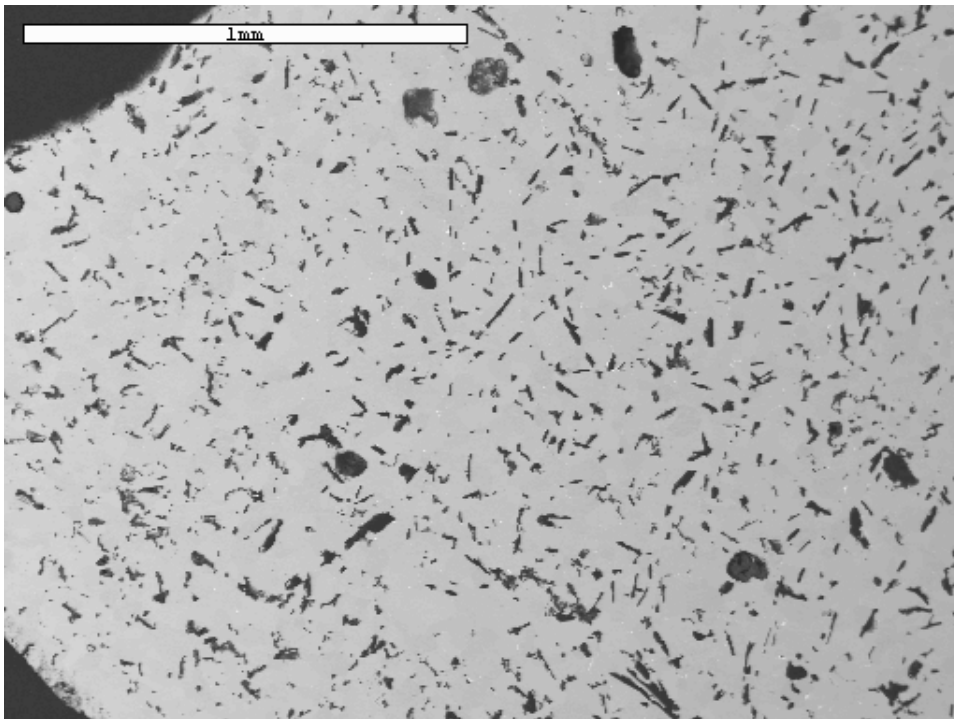


Figure 4-47. TRI-C4 BSE image of post-HHT specimen

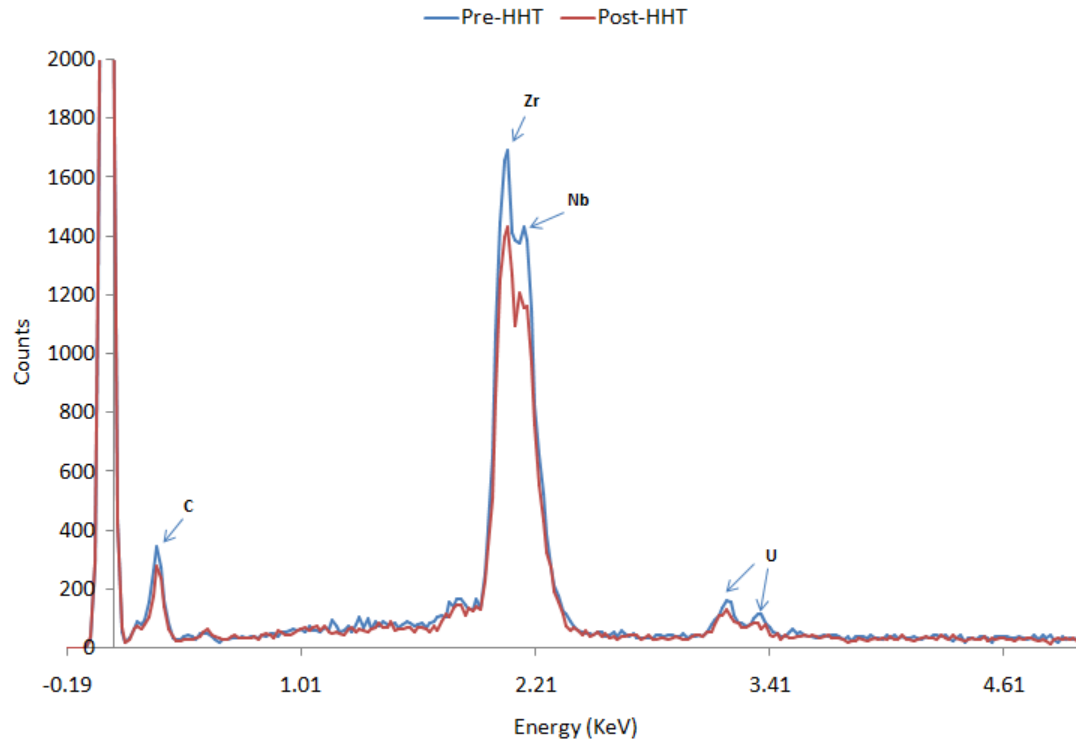


Figure 4-48. TRI-C1 pre- and post-HHT EDS

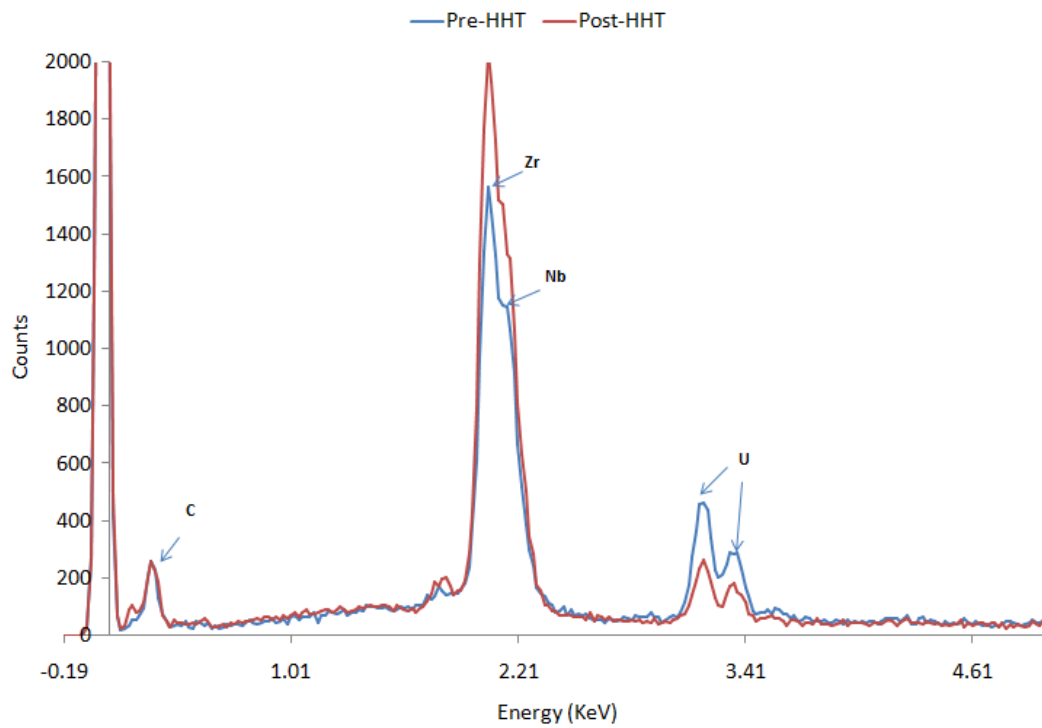


Figure 4-49. TRI-C2 pre-and post-HHT EDS.

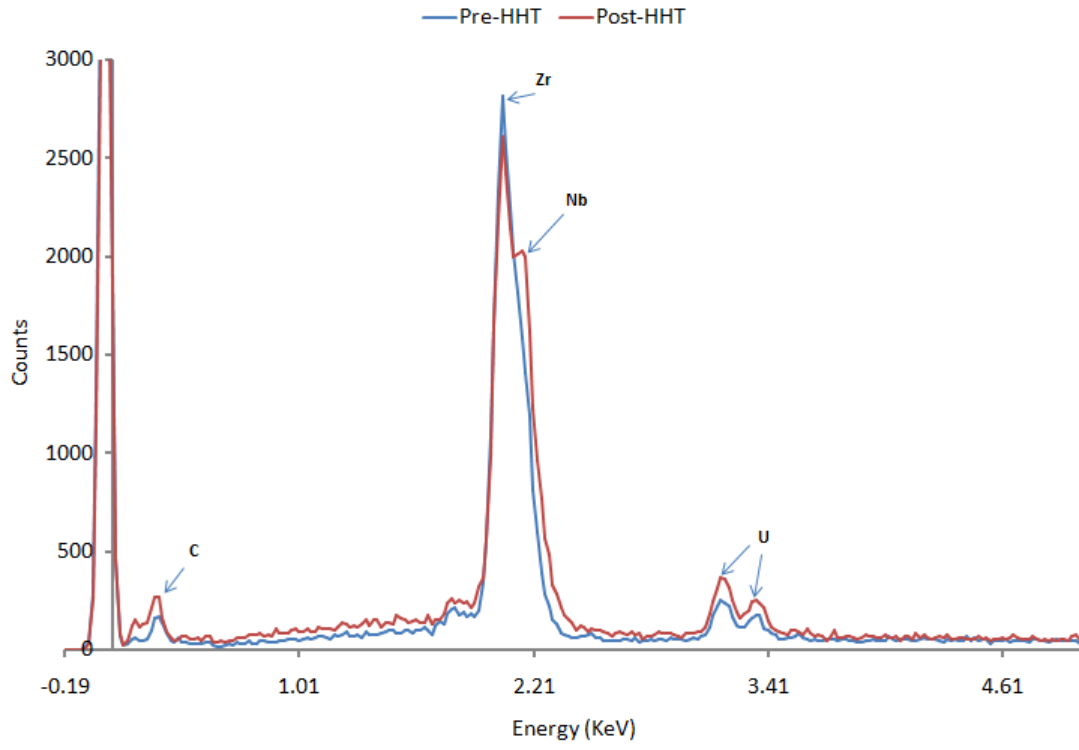


Figure 4-50. TRI-C3 pre-and post-HHT EDS.

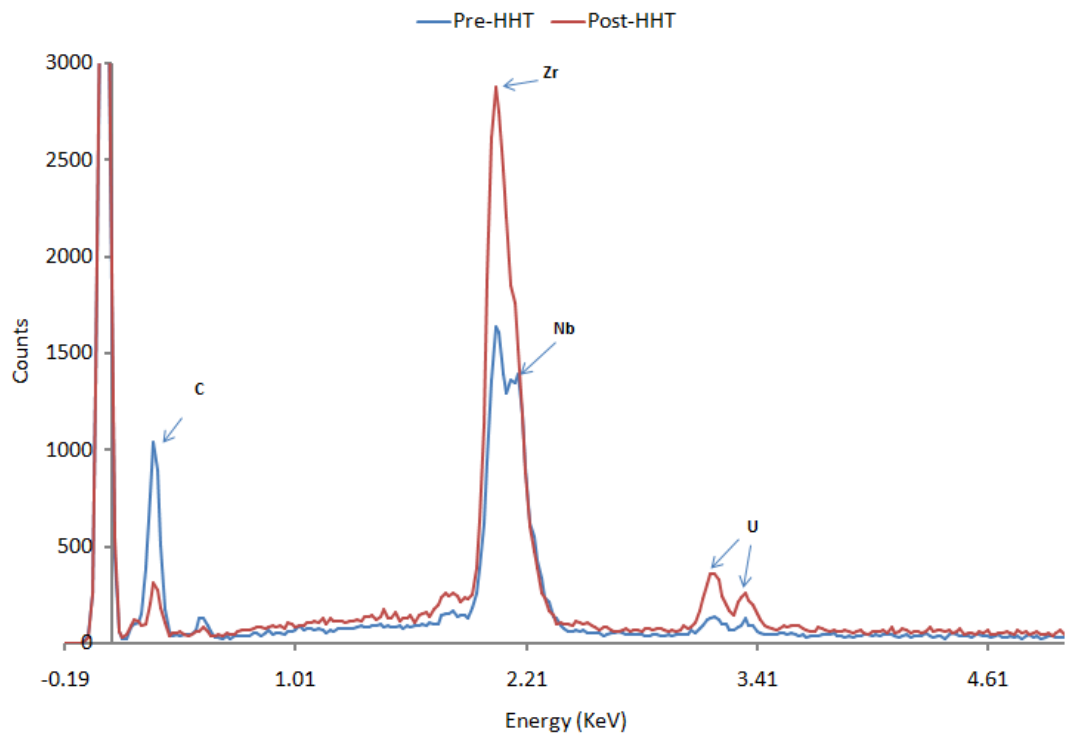


Figure 4-51. TRI-C4 pre-and post-HHT EDS

## CHAPTER 5 CONCLUSIONS AND RECOMMENDATIONS

Testing the mono-carbides, WC, TaC, and ZrC, in a hot hydrogen environment yielded different results depending on the carbide composition. The sample that had the least change in microstructural integrity was the ZrC sample. The sample's carbon content remained the same. No cracking, grain growth, density changes, or hydrogen embrittlement was observed. The XRD spectrum showed the post-HHT specimen to have no change in phase from the pre-HHT specimen.

The TaC post-HHT sample performed the second best in having minimum degradation on the microstructural integrity. There was no depletion of carbon from the sample, both bulk and cross-sectional; however, the sample did experience extensive cracking. A density decrease of 4.836% in the post-HHT sample was measured against the pre-HHT sample.

The WC sample performed the worst in a hot hydrogen environment. The post-HHT sample experienced a noticeable degree of phase change, grain boundary separation, carbon depletion, and possible formation hydrocarbons. Portions of the post-HHT sample's XRD spectrum showed the formation of  $W_2C$ .  $W_2C$  most likely formed on the edge where carbon depletion occurred. After a two hour test at 2775K, the hydrogen was shown to deplete carbon from the WC matrix at rate of  $5.25 \mu m / \text{min}$ . WC also experienced the greatest change in density, decreasing by 10.91%. Based on these results WC would not be a safe fuel candidate for NTP because of the threat of fuel failure due to changes in the microstructure.

Testing of the four solid solution uranium tri-carbides was also conducted at higher temperatures (approximately 2900K) for two hours, representative of NTP operating time. Analysis showed the tri-carbides displayed little to no evidence of changes due to the hot hydrogen environment. The bulk carbon analysis showed that three of the four carbides

displayed constant carbon content from pre- to post-HHT status. The fourth tri-carbide sample reported a loss in carbon content. This was most likely due to carbon contamination during processing and handling of the specimen. The SEM images showed no regions of microstructural segregation with particular attention given to the surface since the surface is where the depletion of carbon would be the greatest. The XRD patterns verified the SEM and bulk carbon analysis by showing that the tri-carbide specimens remained as unaffected solid solution carbides. Based on the analysis, solid solution uranium tri-carbides appear to be compatible with hydrogen to a maximum tested temperature of 2926K for two hours.

Hydrogen corrosion due to temperature is only one mechanism that can affect the rate at which hydrogen can attack a fuel matrix. Future work investigating carbides and more importantly tri-carbides as NTP fuel should examine the effects of other corrosion mechanism such as fuel irradiation. Since the hot hydrogen corrosion process consists of temperature effects coupled with radiation exposure and thermal mechanical stresses, future tests should attempt to incorporate multiple corrosion mechanisms.

## LIST OF REFERENCES

- [1]. T. W. Knight, "Processing of Solid Solution Mixed Uranium/Refractor Metal Carbides for Advanced Space Nuclear Power and Propulsion Systems" Ph.D. Dissertation, University of Florida, Gainesville, FL 2000.
- [2]. S. Anghaie, T. W. Knight, "Development of Robust Tri-carbide Fueled Reactors for Multi-Megawatt Space Power and Propulsion Applications", American Nuclear Society 2004 Winter Meeting, Washington D.C., 2004.
- [3]. D. P. Butt, D. G. Pelaccio, M. S. El-Genk, "A Review of Carbide Fuel Corrosion for Nuclear Thermal Propulsion Applications", 11<sup>th</sup> Symposium of Space Nuclear Power and Propulsion Conference, Albuquerque, NM, 1994.
- [4]. Pewee Reactor Test Report, Los Alamos National Laboratory August 1969.
- [5]. D. R. Koenig, "Experience Gained from the Space Nuclear Rocket Program (Rover)", Los Alamos National Laboratory, May, 1986.
- [6]. D. G. Pelaccio, M. S. El-Genk, D. P. Butt, "Hydrogen Corrosion Consideration of Carbide Fuel for Nuclear Thermal Propulsion Applications", Journal of Propulsion and Power, Vol. 11 No6, November 1995.
- [7]. S. I. Sandler, Chemical and Engineering Thermodynamics 3<sup>rd</sup> Ed., John Wiley & Sons, Inc., NY, 1999.
- [8]. NIST-JANAF Thermochemical Tables, 3<sup>RD</sup> Ed., 1985.
- [9]. NIST-JANAF Thermochemical Tables, 4<sup>TH</sup> Ed., 1998.
- [10]. W. F. Seng, P. A. Barnes, "Calculations of Tungsten Silicide and Carbide Formation on SiC using the Gibbs Free Energy" Material Science and Engineering B, Elsevier , Vol. 72 Issue 1, March 2000.
- [11]. JCPDS International Centre for X-Ray Diffraction Data. *Standard X-Ray Diffraction Powder Patterns from the JCPDS Research Associateship.* s.l., Newtown Square, PA, 1996.
- [12]. Boeing Aerospace Company, "Advanced Propulsion Systems Concepts for Orbital Transfer Study", NASA MSFC, Huntsville, AL, 1981
- [13]. T. W. Knight, S. Anghaie, "Processing and Fabrication of Mixed Uranium/Refractory Metal Carbide Fuels with Liquid-Phase Sintering", Journal of Nuclear Materials, Elsevier, Vol. 306, 2002
- [14]. B. Panda, R. R. Hickman, S. Sandeep, Solid Solution Carbides are the Key Fuels for Future Nuclear Thermal Propulsion", NASA MSFC, Huntsville, AL, 2005

- [15]. D. A. Porter, K. E. Easterling, Phase Transformation in Metals and Alloys 2<sup>nd</sup> Ed., CRC Press, Boca Raton, FL, 1992.
- [16]. C. R. Wang, J. M. Yang, W. Hoffman, “Thermal Stability of Refractory Carbide/boride Composites”, *Materials, Chemistry and Physics*, Elsevier, Vol. 72 Issue 3, March 2002.
- [17]. R. Zee, B. Chin, J. Cohron, “Hot Hydrogen Testing of Refractory Metals and Ceramics” Auburn University, Auburn, AL, February 1993.

## BIOGRAPHICAL SKETCH

Brandon Warren Cunningham was born in 1983. He was raised in Mount Dora, Florida. He graduated sum cum laude from Mount Dora High School in May 2001. Brandon attended the University of Florida and majored in nuclear engineering. During the summer of 2006, Brandon received a fellowship with the Center of Space Nuclear Research at Idaho National Laboratory. He graduated with his bachelor's degree from the Nuclear and Radiological Engineering Department at the University of Florida in December 2006.